BULLETIN DE L'ASSOCIATION MINÉRALOGIQUE DU CANADA

THE CANADIAN MINERALOGIST

JOURNAL OF THE MINERALOGICAL ASSOCIATION OF CANADA

Volume 43 April 2005 Part 2

The Canadian Mineralogist
Vol. 43, pp. 513-542 (2005)

MICROSTRUCTURES OF COMMON POLYGONAL SERPENTINES FROM AXIAL HRTEM IMAGING, ELECTRON DIFFRACTION, AND LATTICE-SIMULATION DATA¶

ALAIN BARONNET§

CRMCN–CNRS, Campus Luminy, Case 913, F–13288 Marseille Cedex 09, France*

BERTRAND DEVOUARD§

Département des Sciences de la Terre, UMR 6524 OPGC – CNRS – Université Blaise Pascal, 5, rue Kessler, F–63038 Clermont-Ferrand Cedex, France

ABSTRACT

Imaging with high-resolution transmission electron microscopy (HRTEM), selected-area electron diffraction (SAED), and numerical simulations of the diffraction patterns are combined to further document the microstructures of the most widespread types of 15-sector and 30-sector polygonal serpentines. Imaging, diffraction and simulation data recorded along the fiber axis are reconciled with a model involving lateral continuity of the 1:1 layer structure and a curvature without inversion of the sheets of tetrahedra across the sector boundaries. Axial fivefold symmetry is confirmed for polygonal serpentines. This model differs from sharp-boundary models proposed by Chisholm (1991, 1992), without inversion, and by Dodony (1993, 1997a), with inversion. Streaked diffraction chords connecting Bragg reflections are typical of all polygonal fibrils. They are due to curved layers with constant curvature at sector boundaries, involving extra spacing and locally distorted H-bonds between layers. This is a peculiarity of polygonal serpentines, not present in other varieties of rolled serpentine.

Keywords: serpentine-group minerals, polygonal serpentine, microstructure, HRTEM, electron diffraction, dislocation, fast Fourier transform.

SOMMAIRE

La microscopie électronique à transmission à haute résolution (METHR), la diffraction électronique sur aire sélectionnée, ainsi que des simulations numériques des clichés de diffraction, ont été combinées pour progresser dans la connaissance des microstructures des types les plus répandus de serpentines polygonales à 15 et 30 secteurs. Imagerie, diffraction et simulations sont en bon accord avec un modèle intégrant la continuité latérale des feuillets 1:1 et une courbure sans inversion de polarité aux jonctions des secteurs. Une symétrie axiale d'ordre cinq est confirmée pour les serpentines polygonales. Ce modèle diffère des modèles proposés par Chisholm (1991, 1992), avec des jonctions anguleuses et sans inversion, et par Dodony (1993, 1997a), avec inversion. Des trainées diffuses joignant les réflections de Bragg sont typiques de toutes les fibres polygonales. Elles sont dues à

§ *E-mail addresses*: baronnet@crmcn.univ-mrs.fr, devouard@opgc.univ-bpclermont.fr

¶ We dedicate this article to the memory of Sturges William Bailey (1919–1994) and Boris Borisovich Zvyagin (1921–2002), both major investigators of serpentine-group minerals and other layer silicates.

* Also associated with the Universities of Aix-Marseille II et III.

la courbure des feuillets avec un rayon de courbure constant aux jonctions des secteurs plans, impliquant un sur-épaississement basal et une distorsion locale des liaisons hydrogène interfoliaires. Ceci est une particularité des serpentines polygonales par rapport aux autres variétés enroulées.

Mots-clés: serpentine polygonale, microstructure, METHR, diffraction des électrons, dislocation, transformée de Fourier rapide.

Introduction

Lizardite, chrysotile and antigorite are the three most common structural varieties of the trioctahedral family of 1:1 layer silicates (*e.g.*,Wicks & O'Hanley 1988). Except for the introduction of a talc component in antigorite, their chemical formula does not depart much from the $Mg_3Si_2O_5(OH)_4$ end-member composition. However, they cannot yet be considered as true polymorphs because neither experimental studies nor petrological observations have clearly ascribed stability fields to each of these structural modifications. Moreover, they coexist commonly as complex intergrowths, as shown by many recent studies of serpentinites by transmission electron microscopy (TEM) (*e.g.*, Baronnet & Belluso 2002, Baronnet & Devouard 1996, Belluso *et al*. 1998, Mellini 1986, Spinnler 1985).

Polygonal serpentine (PS) or "Povlen-type chrysotile" was early recognized as another rolled microstructure of serpentine (*e.g.*, Cressey 1979, Cressey & Zussman 1976, Mellini 1986, Middleton & Whittaker 1976, Mitchell & Putnis 1988, Yada & Liu 1987). The description of the detailed structure of both 15- and 30-sector PS is needed to place PS among other serpentine varieties (Wicks & O'Hanley 1988). The interpretation of partial results of more recent microstructural studies remain controversial (Baronnet *et al.* 1994, Chisholm 1992, Dodony 1997a) and, therefore, needed to be documented further.

Our aim in this paper is thus to document microstructural data from high-resolution electron imaging and electron diffraction of polygonal serpentine with 15 and 30 sectors. Numerical simulation techniques of the diffraction features are used to interpret the results. Such data are required to help provide the missing crystallographic details of the structure. Finally, we discuss the previous models in the light of these results.

Experimental

Samples

Serpentinite specimens are from: i) the Piemont Zone (Alps), Italy, kindly supplied by E. Belluso (University of Torino), ii) La Carrade Quarry (Hercynian Maures Massif), Var, France, iii) the Costabonne mine, Pyrénées, France, iv) the Jeffrey mine, Québec, Canada, and iv) drill core from midoceanic crust. Serpentine veins or serpentinite matrix containing mutually disoriented fibers are here preferred over those with a strongly developed asbestiform texture. Although the latter may display hundreds of parallel fibrils at a time, the former display PS with free-grown outlines, and a rather clean diffraction pattern may be recorded from these without too much interference from reflections produced by their neighbors.

After having examined the growth features of several hundreds of PS fibrils from various geological contexts, over a period of some ten years, we have found that the PS can display a great microstructural variability. However, the most common fibrils are those reported on below. We leave the description of deviant forms for a furture article.

Specimen preparation for TEM

Fifty-micrometer-thick thin sections were cut normal to vein surfaces and glued on a glass slide with Lakeside or CrystalBond thermal resin. A disk 3 mm in diameter was drilled with an "O. Medenbach" microdrill fitted to a polarizing microscope. Then a single-hole TEM copper grid (usually 2 × 1 mm slot) was glued on top of the disk-shaped section with an ultrathin layer of epoxy resin, and allowed to polymerize overnight. The grid–rock disk assembly was then detached from the glass slide with a TEM tweezer after gently melting the resin underneath with the tip of a soldering iron. The glue adhering to the disk was washed away with several baths in ethanol, and the disk was then ready for ion-thinning. A Gatan 600, or PIPS, ion mill with paired ion guns was used for thinning at room temperature. On the Gatan 600, the first 5 hours of thinning were done at 5 kV, 25 nA with 20° incidence, and the last 10 hours, until a hole formed, were done at 3–4 kV, 25 nA with 12° incidence. The preparation was finished at 2 kV to minimize the amorphous film on both sides of the specimen. On the PIPS ion mill, incidence angles were typically 4° on the specimen side and 9° on the grid side, and the total thinning time was reduced to *ca*. 2–3 hours. The specimen preparation was finished after coating it with a rather thick (20 nm) layer of amorphous carbon to insure good conduction of electrons between the tubular microstructures and the copper grid in the microscope.

Electron microscopy

A JEOL 2000 fx transmission electron microscope operated at 200 kV, located at CRMC–N (part of the CNRS/INSU French National TEM facility), was used to acquire most of the images and the electron-diffraction data presented here. Point-to-point resolution in

image mode is 0.28 nm. An attached Tracor TN 5502 EDX microanalytical system allowed us to check mineral compositions, but they are not reported here. The best-resolved (0.20 nm) micrographs presented in this paper were obtained on a JEOL 4000 fx at the RUCA–EMAT Antwerp TEM facility, and some others on a JEOL 3010, also at the CRMC–N facility. A TV-rate, high-sensitivity camera (LHESA) was systematically used during the object-orientation procedure and the setup of optimum conditions for imaging . This procedure minimized electron-radiation damage. The full-beam conditions were re-established slowly and only to record the micrographs. Local charging on the specimens and drift were dealt with by correcting the objective lens astigmatism after any change in tilt.

A ±30° double-tilt specimen stage was used for precise orientation of the fibers. The axial orientation of a fiber was first approached in direct space by rotating it at constant speed using the axial tilt of the specimen holder under perfectly eucentric conditions. Then the rotation was stopped at the point where the diffraction "contrast cross" rotated on the fiber image at maximum angular speed. Eventually, we used the transversal tilt to spread the cross to make the fiber completely black, *i.e.*, maximum diffraction contrast over the entire cross-section was obtained. The diffraction mode was used to finalize the orientation.

The best high-resolution images were recorded at relatively low magnification of 150,000 to 300,000× to minimize electron doses, and in the thinnest regions. Only one to three through-focus micrographs were usually taken, bracketing the Scherzer defocus, before the fiber became amorphous. No image-enhancement technique (such as averaging or Fourier transform filtering) was used on the HRTEM micrographs presented here.

Techniques of direct space and reciprocal space simulations

In the case of cylindrical lattices, the correspondence between image contrasts and diffraction features is not easily explored by standard techniques of dark-field imaging. Diffraction beams or streaks cannot be selected individually because of the ubiquitous overlap of diffraction features coming from different sectors. Therefore, simulations of the lattices of regular polygonal serpentines and of their associated diffraction-patterns proved necessary to interpret the complex observations in both spaces. These simulations are reminiscent of those conducted for chrysotile (Devouard & Baronnet 1995), but here they have been extended to the polygonal case.

First, a special algorithm was designed to draw curved and flat Bravais lattice nodes projected along [100], *i.e.*, onto the (100)* reciprocal plane common to all flat sectors. Both fifteen or thirty sectors were considered, and the layer structure of the serpentine was assumed to be laterally continuous, without reversal of polarity across sector boundaries. Each layer closes up as an integral number of Bravais unit-cells with five more unit-cells added per new adjacent outer layer (Jagodzinski & Kunze 1954, Yada 1967). In addition, the continuity of individual layers across sector boundaries was secured through curved portions of the layers, which stack while keeping a constant radius of curvature from one layer to the next. In these portions, the mechanically neutral surface is located in the middle of the serpentine single layer, *i.e.,* roughly along the apical O – inner-OH plane connecting the sheet of tetrahedra to the sheet of octahedra. The lizardite mode of stacking successive layers was assumed to apply inside the sectors, *i.e.*, optimal H-bonding exists between the flat layers. These conditions are those contained in the model proposed by Baronnet *et al.* (1994). Accordingly, each fiber was made of a rotational set of sectors (15 or 30) with fully coherent junctions between successive layers.

Input variables for generating a polygonal fiber were: i) the number of sectors, ii) the inner core diameter, iii) the number of layers making the fiber wall (up to 60 layers, *i.e.*, modeling fibers up to 42 nm in diameter), iv) the stacking sequence (periodic or semirandom) within one of the sectors, the others being automatically generated from the layer-continuity principle, and v) the radius of curvature inside sector boundaries, which controls the sector-boundary width.

The resulting dot patterns were represented by 1024 × 1024 or 2048 × 2048 pixel matrices. Then a fast Fourier transform (FFT) algorithm was applied to generate the topology of the diffraction pattern as its power spectrum. Because the actual structure of a single layer of serpentine was not introduced in the computation (only lattice nodes were considered), the topology of the Fourier space is correct, but the structure factors are not taken into account, and thus intensities may not be accurate. However, diffracted intensities are not essential, as they can be modified by numerous factors, including dynamic diffraction conditions, misorientations, and the unequal development of sectors.

Precautions were taken to reduce the artifacts inherent to FFT techniques. Nevertheless, a few residual artifacts can be recognized in the power spectra, such as faint streaking around 00*l* reflections or exaggerated elongation of basal reflections for 30-sector fibers. Both are due to the shape factor of the limited sectors, and low-intensity spots in the background that come from aliasing (folding over of high-frequency intensities).

Results: TEM Images of Regular Fibers

Bright-field zone-axis images of 15- and 30- sector fibers are shown at low magnification in Figures 1 and 2, respectively. They are most representative of regular fibers, *i.e.*, those with nearly equal radial development of component sectors. The outer diameter of most fibers of polygonal serpentine extends from 40–50 nm to

beyond one micrometer. The hollow core may vary in diameter from very small (2 nm or less) to several hundreds of nanometers. This is in contrast with chrysotile cylinders, whose inner diameter is rarely below 5 nm and the outer diameter rarely above 65 nm (Yada 1967, 1971). Coreless polygonal fibers have isosceles triangular sectors that may or may not radiate out from a unique point. In all cases, however, both intersector angles and the angles between adjacent (001) lattice planes retain regular values of 24° and 12°, for 15 sectors and 30 sectors, respectively (Figs. 3a, b). Cylindrical and spiral wrapped (polygonal scrolls) serpentine layers coexist among fibers of the same occurrence. The spiral pitch is usually one to several layers thick, but rare "ammonite-like" fibers may have pitches of several tens of serpentine layers.

Sectors are made of a lizardite-like material. Flat 1:1 layers are tangential to the fiber [*i.e.*, (001) // fiber axis] and parallel to their own external sector "facet". High-resolution images of these flat parts of the microstructure cannot be distinguished from those of lizardite seen along any of the three *xi* – <100> type directions (Fig. 3), as defined by Bailey (1988). Bright spots, 0.45 nm apart along the layering, display shifts of possible 0 or ±0.15 nm along the layer trace in going from one layer to the next. The stacking sequences of these shifts along the normal to the layers may be regular (Fig. 3a) or semirandom (Fig. 3b), suggesting ordered and disordered polytypes, respectively.

Structural continuity is invariably observed between adjacent sectors. This is particularly evident in PS fibers with overall ordered sequences, in which stacking faults can be followed from one sector to both the adjacent ones (Fig. 4). Modifications of the stacking sequences from one sector to the next also are obvious in the high-resolution images. For ordered sequences, these

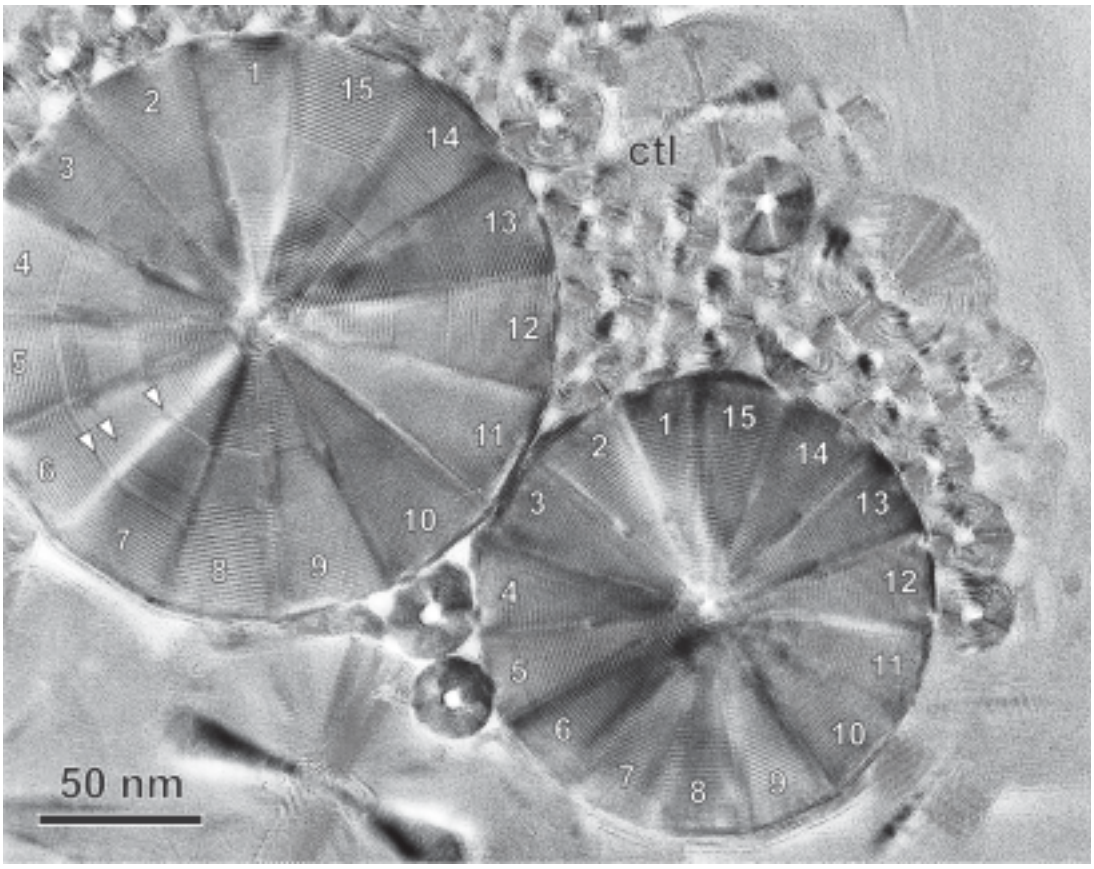

FIG. 1. Low-magnification HRTEM bright-field image of cross-sections of two regular 15-sector fibrils of polygonal serpentine (15-PS) seen along the [100] axis, and surrounded by chrysotile fibers. The bottom-right PS is built up of a two-layer polytype, whereas the one in the upper left mixes two-layer and one-layer stackings. Arrowheads mark stacking faults. "Picrolite" from the Jeffrey mine, Québec (JEOL 3010).

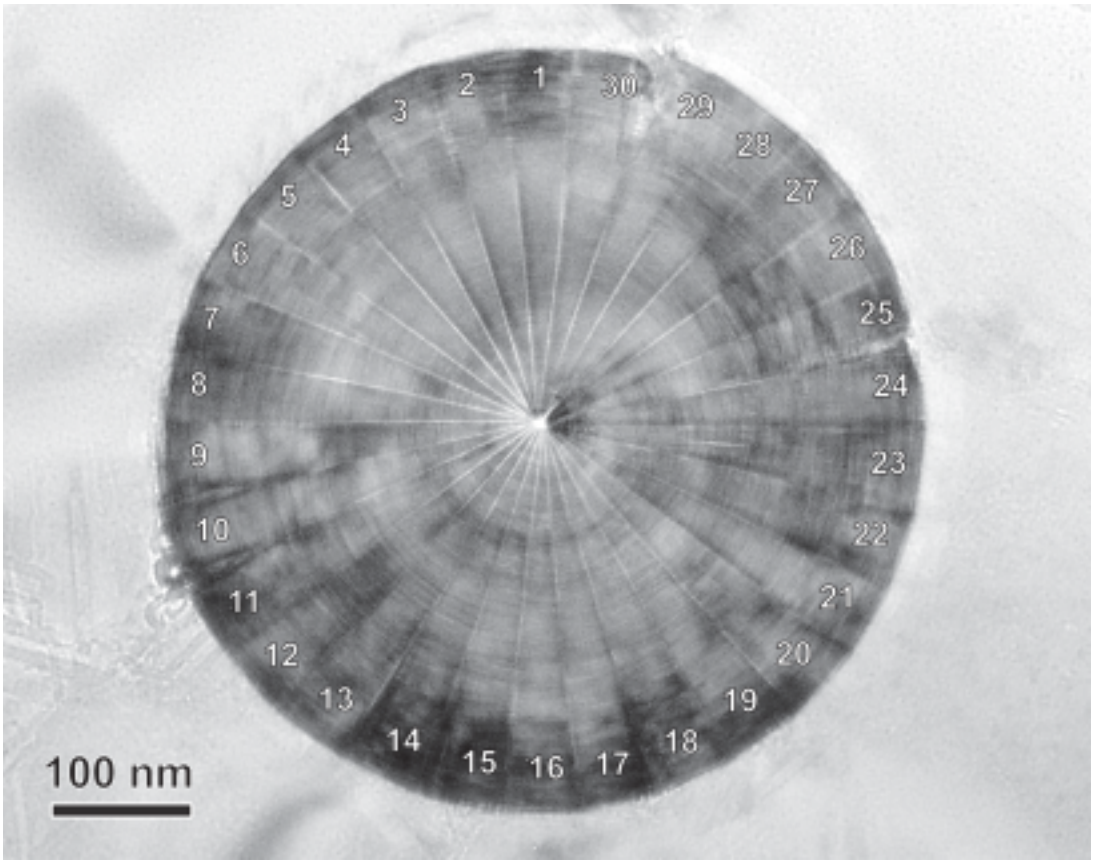

FIG. 2. Low-magnification TEM bright-field image of a regular 30-sector fibril of polygonal serpentine (30-PS) seen along its [100] axis. Note the defective rim between sectors 29 and 30, presumably due to the imperfect closure of the fiber along this plane at the end of growth. Overfocusing of the objective lens emphasized the contrast between sectors. Serpentinite vein from the Piemont zone, Western Alps, Italy. JEOL 2000FX. The SAED pattern is derived from the fiber shown in Figure 19.

modifications commonly result in a succession of orthogonal (O), right-slanted (R) and left-slanted (L) unit-cells (in 2D projection) in successive sectors (Fig. 4), repeating every three sectors. This succession was first described by Dodony (1993, 1997a) in ordered 30-sector fibers. In some cases, a non-equivalent but regular structural repeat every three sectors can be seen on low-magnification micrographs by uneven electron-beam-induced damages between or within sectors (Fig. 5). Further information on stacking sequences in sectors will be provided below, on the basis of diffraction space.

Not only the regular fibers, but all the hundreds of fibers we examined thus far exhibit curved junctions of (001) lattice planes through sector boundaries when properly aligned and seen at sufficient magnification, as in Figures 3 and 4. The radius of curvature of roughly 10–15 nm for both 15- and 30-sector fibrils is constant or nearly so from the core to the rim of most fibrils (Fig. 3). This uniformity ensures a locally constant width of the sector boundary. This width tends to be larger in 15-sector fibers (4 to 5 nm) than in 30-sector fibers (2.5 to 3 nm) because the kink angle between (001) lattice planes in the former case is twice that in the latter case. Such constant curvature results in a progressively larger flat part in each layer-turn from core to rim. Small hollow cores are limited by rounded layers where the curved 15- or 30-sector boundaries meet. This progressive evolution from mostly curved to mostly flat layers outward avoids structural disruption of crystal matter, as would be expected from the model of Middleton & Whittaker (1976) of an abrupt polygonal coating over a core of chrysotile fiber. From our observations, a distinct cylindrical core is not generally present in most cases of PS observed thus far.

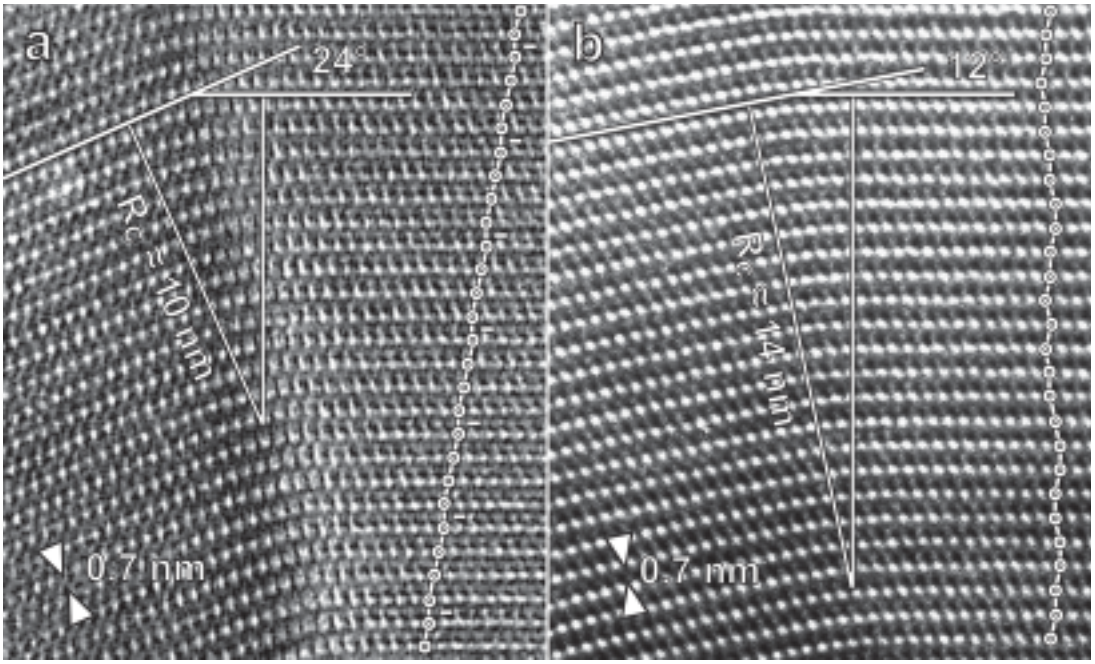

FIG. 3. HRTEM two-dimensional images of the boundary between two consecutive sectors of fibrils of polygonal serpentines. White spots, 0.45 nm = *b*/2 apart along the layers indicate a [100]-type zone-axis for both images. The structural continuity between consecutive sectors is ensured by a layer curvature. a) A 15-PS with a four-layer stacking sequence. Note how the +++ shift sequence on the right sector converts to a 000 shift sequence on the left, *i.e.*, the structure undergoes a homogeneous shear. "Picrolite" from Jeffrey mine, Québec. Raw image. JEOL 3010. Raw image. b) A 30-PS fibril with a semirandom sequence of stacking. La Carrade quarry, Var, France. Raw image. JEOL 4000ex.

On properly oriented high-resolution micrographs, no evidence of polarity reversal can be seen between sectors, for 15- or 30-sector PS, even on high-resolution images, where sheets of tetrahedra and of octahedra can be resolved (Fig. 3a).

RECIPROCAL-SPACE SIMULATIONS OF REGULAR FIBERS

The interpretation of the axial diffraction-patterns produced by single fibers (see Figs. 15 and 16, below) has been made possible using a progressive simulation approach. In this section, structural ingredients of the fiber are introduced progressively in the simulation so that the origin of the various diffraction features may be identified in direct space.

The diffraction pattern is assumed to be the sum of the diffraction features issued from individual parts of the fiber. This statement is not correct for the usual case of a translation lattice, where strong phasing exists among the different parts of an object. However, this situation may work to simulate cylindrical lattices, for which translational phasing is relaxed. In other words, we have made the unconventional assumption that the Fourier transform of the fiber as a whole is the sum of the Fourier transforms of component building parts of the fiber, such as individual sectors and junctions at sector boundaries. Such an assumption had been used successfully by Devouard & Baronnet (1995) for chrysotile. In that case, the axial diffraction-pattern of the circular object could be geometrically predicted as the sum of the reciprocal lattices of local translation-lattices as polygonal approximants from all around the cylindrical

FIG. 4. HRTEM two-dimensional images of three consecutive sectors of polygonal serpentines with two-layer polytypes. The stacking sequences of each sector are drawn; their power spectrum derived from FFT of portions of the HR image are shown as insets underneath. Arrowheads point to the same stacking fault crossing consecutive sectors. Note the changes of direct and reciprocal unit-cells when going from one sector to the next one (see text for detailed discussion). a) A 15-sector PS. "Picrolite" from the Jeffrey mine, Québec. Raw image. JEOL 3010. b) A 30-sector PS. La Carrade quarry, Var, France. Raw image. JEOL 4000ex.

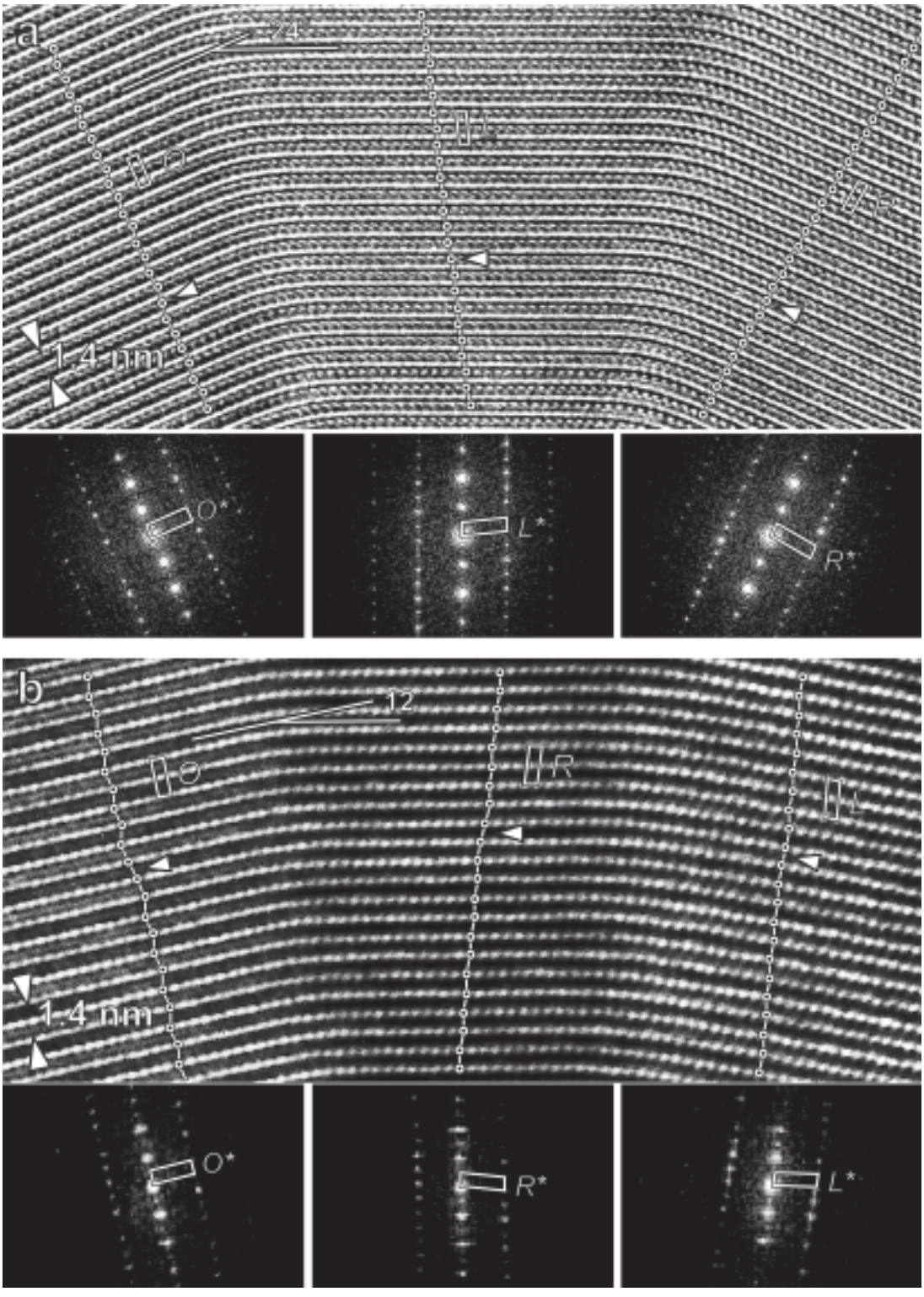
a
24
O
R
L
1.4 nm
O*
L*
R*
b
12
O
R
L
1.4 nm
O*
R*
L*

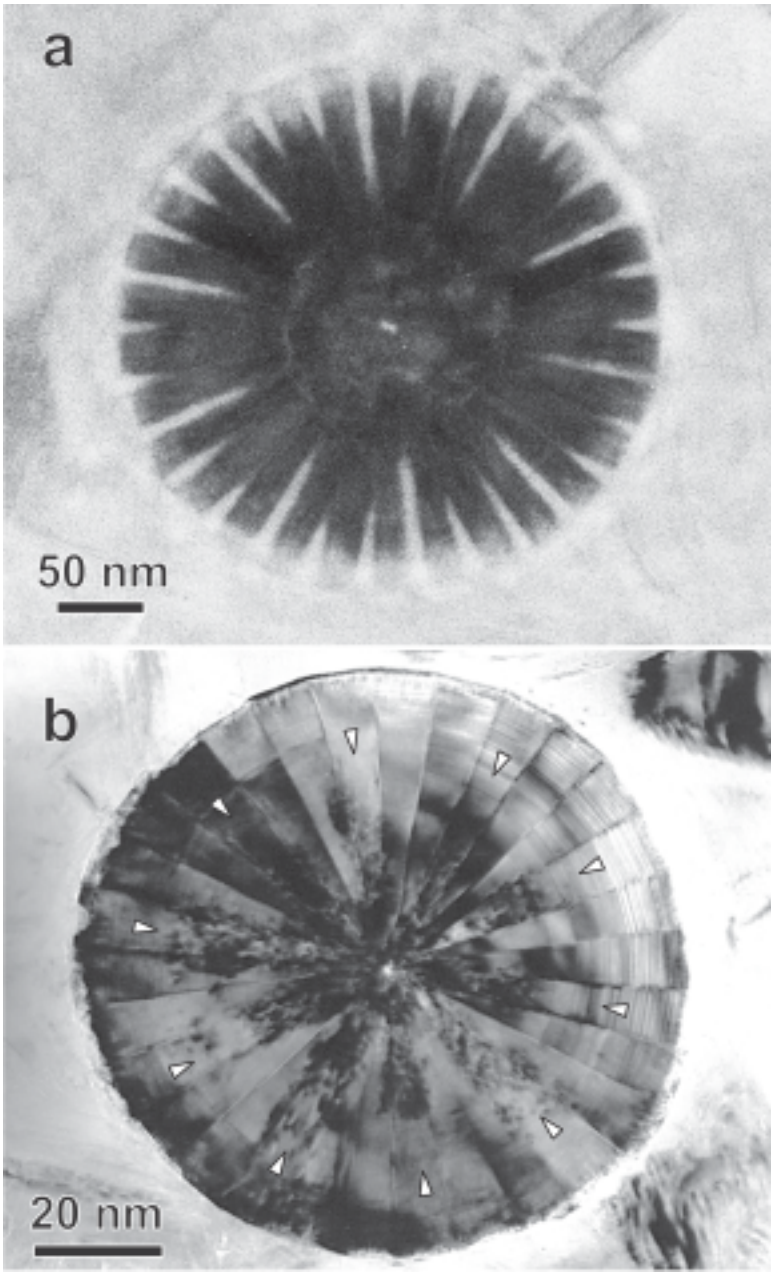

FIG. 5. Low-magnification images of selective electron damages on 30-sector PS fibers. a) The contrast in the "serpentine clock" dial is due to silicate amorphization at curved sector boundaries. The apparent periodicity over three boundaries is considered to be caused by the contact between right (*R*)- and left (*L*)-leaning unit-cells of neighboring sectors (long trace) that differ from the two enantiomorphous *L–O* and *R–O* contacts (short traces).The latter should have the same boundary-structure, and therefrom the same sensitivity to beam damage. Such a pattern occurs in fibers with fully ordered, low-repeat sequences of stacking. Semirandom stacking, for which beam damage might be equalized among successive boundaries, should not cause such a pattern. Piemont serpentinite, Western Alps, Italy. b) Mottled contrasts periodically distributed within one out of three sectors (white arrowheads). An orthogonal (*O*) unit-cell is expected for such damaged sectors because the other *L* and *R* sectors might behave similarly as enantiomorphous variants of the same structure. La Carrade quarry, Var, France.

fiber. For polygonal serpentines, the procedure consists in the following steps: i) recall the basic features of the <100> diffraction pattern of lizardite as the model for diffraction of a single sector; ii) then build up three of these lizardite-like sectors after considering proper structural shifts, sector shapes, rotations, and suitable curved junctions between sectors, and iii) finally propagate the results over a full turn to complete the fiber as a whole.

The <100> SAED pattern of lizardite

Two-dimensional numerical Fourier transforms of three polytypes of lizardite are reported in Figure 6, using primitive lattice nodes of the projected subcells as a numerical mask for multilayer polytypes. The resulting power spectrum may be compared with a SAED pattern provided that single-layer structure-factors and conditions of dynamic diffraction are neglected. Bailey & Banfield (1995) and Dodony (1997b) published simulations of the SAED patterns of various polytypes of lizardite under conditions of dynamic diffraction.

In all diffraction patterns, diffraction rows, parallel to [001]* and $(0.45\ \text{nm})^{-1}$ apart, are successively indexed as [0 0 *l*]*, [0 ± 2 *l*]*, [0 ± 4 *l*]*, [0 ± 6 *l*]*, *etc.*, the missing rows being due to the *C*-centering of the Bravais cell of such layer silicates. Regular polytypes and semirandom stackings show up as supercell spots

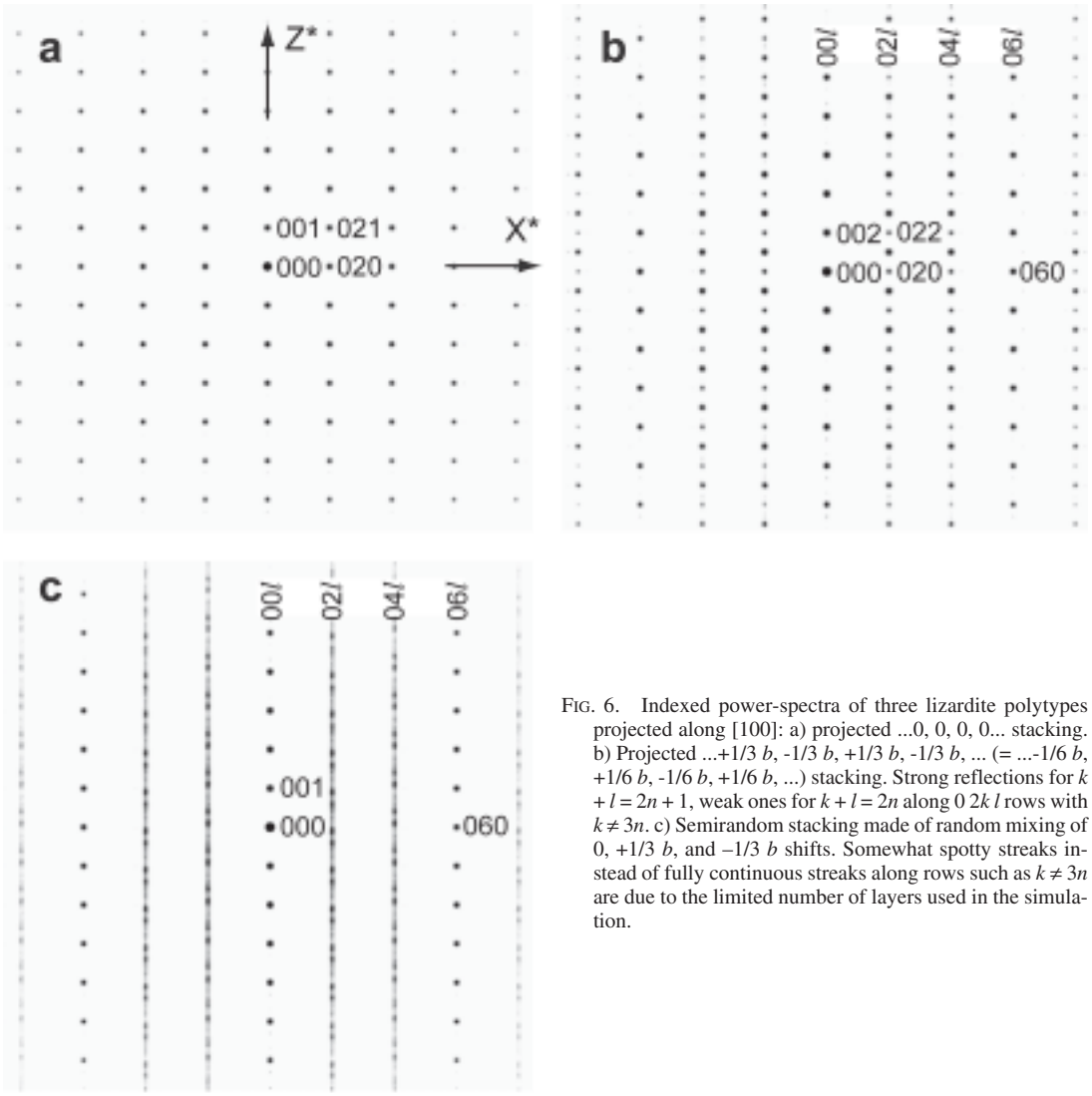

FIG. 6. Indexed power-spectra of three lizardite polytypes projected along [100]: a) projected ...0, 0, 0, 0... stacking. b) Projected ...+1/3 *b*, -1/3 *b*, +1/3 *b*, -1/3 *b*, ... (= ...-1/6 *b*, +1/6 *b*, -1/6 *b*, +1/6 *b*, ...) stacking. Strong reflections for $k + l = 2n + 1$, weak ones for $k + l = 2n$ along 0 2*k l* rows with $k \neq 3n$. c) Semirandom stacking made of random mixing of 0, +1/3 *b*, and –1/3 *b* shifts. Somewhat spotty streaks instead of fully continuous streaks along rows such as $k \neq 3n$ are due to the limited number of layers used in the simulation.

or streaks along [0 ± 2 *l*]*, [0 ± 4 *l*]*, [0 ± 8 *l*]*, [0 ± 10 *l*]*, *i.e.*, along [0 2*k l*]* with $k \neq 3n$, respectively. On the other hand, [0 0 *l*]*, [0 ± 6 *l*]*, *etc*., *i.e.*, [0 2*k l*]* with $k = 3n$ are invariably made of regular spots (0.73 nm)$^{-1}$ apart, that is, they are affected by systematic extinctions. These rows are indicative of the 0, ±⅓(*b*/2) shift operators we used to generate the layer-stacking sequences.

The <100> SAED pattern of a few connected sectors of lizardite

A numerical mask was made for the lattice having the shape of a truncated, isosceles triangle with a 24° (15-sector PS) or 12° (30-sector PS) apex angle. Then we took care of the layer shifts *s* in the generation of the stacking sequence of contiguous sectors. For flexural folding of layer packets, keeping the layer thickness constant, Devouard & Baronnet (1995) showed that $s = t\alpha$, with *t* as the layer thickness and α as the flexure angle in radians. This relation indicates that the glide component along the interlayer space is completely insensitive to the shape of the flexured part but responds to the flexure angle only. Note that constant layer-thickness is indicated experimentally by circular and sharp 00*l* diffraction rings with (0.73 nm)$^{-1}$ radius in the diffraction space, whatever the local curvature and shape of the serpentine layer packets may be.

With *t* = 0.73 nm, α(15 PS) = 24° = 0.42 rd and α(30 PS) = 12° = 0.21 rd, we have: *s* (15 PS) = 0.30 nm ≈ *b*/3, and *s* (30 PS) = 0.15 nm ≈ *b*/6. Accordingly, the stacking sequences of polytypes are "sheared" homogenously by these amounts in going from one sector to the next. This shearing is a direct consequence of the continuity in atomic structure across the sector boundary. Homogeneous shear affecting all interlayers has been envisaged for the 30-sector PS (Amelinckx *et al.* 1996) as a modification of the "coherent layer-pair" model originally proposed by Baronnet *et al*. (1994). Polytypes thus undergo a "martensite-like" modification between successive sectors (Baronnet *et al*. 1994). For [100] projections, the +*b*/3 shift is equivalent to the –*b*/6 shift, and the +*b*/6 shift is equivalent to the –*b*/3 shift, owing to the projected *b*/2 periodicity. The same projected stacking structure will be consequently repeated after three sectors for both 15 PS and 30 PS. This finding justifies using three sectors for the intermediate simulation. In the 3-D structure, the sector sequence will

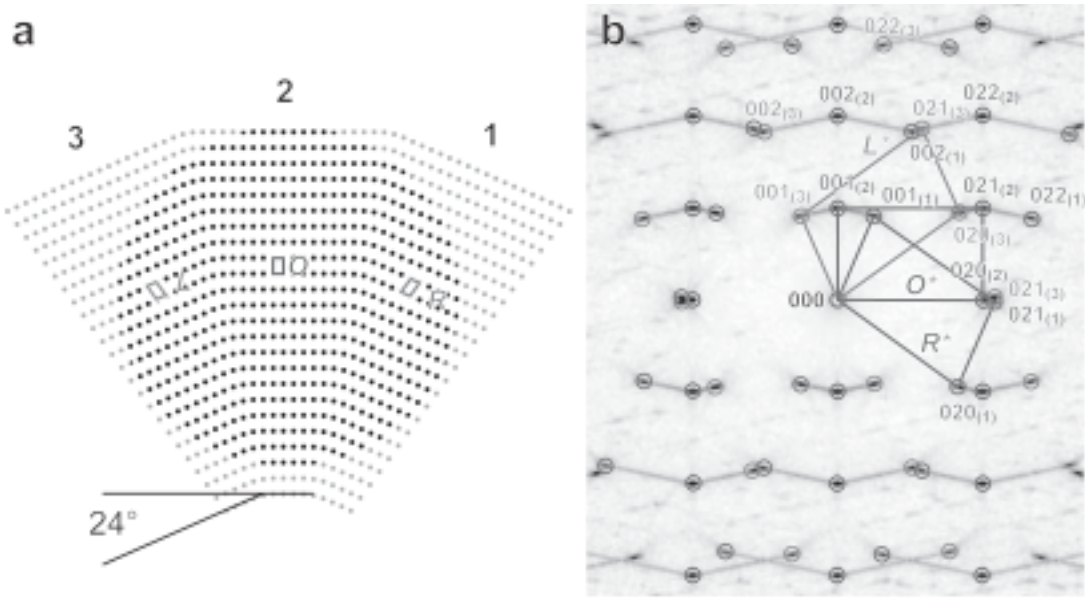

FIG. 7. a) Circular mask of the Bravais lattice nodes of three consecutive sectors of a 15-PS seen along [100] with a ...0, 0, 0, 0, ... projected stacking-sequence, *i.e.,* with an orthogonal (*O*) projected (primitive) unit-cell in sector 2. In neighboring sectors 1 and 3, the "closest-to-orthogonal" convention produces unit cells that are oblique-to-the-right (*R*) and oblique-to-the-left (*L*), respectively. Note how the 0 2*k l* lattice planes in sector 2 deviate only slightly upon crossing sector boundaries. b) Power spectrum (FFT) of Figure 7a. Indexing as 0 *k l* (*i*), with *i* as the sector numbering. Individual reflections are circled in color according to which sector they arise. *R**, *O** and *L** reciprocal-plane unit-cells correspond to the direct-space *R*, *O*, and *L* unit-cells, respectively. Diffuse segments connecting basal reflections [*e.g.,* 0 0 $\bar{1}$ (1), 0 0 $\bar{1}$ (2), 0 0 $\bar{1}$ (3)] and non-basal reflections [*e.g.,* 0 2 0 (1), 0 2 $\bar{1}$ (2), 0 2 $\bar{2}$ (3)] show up quite well.

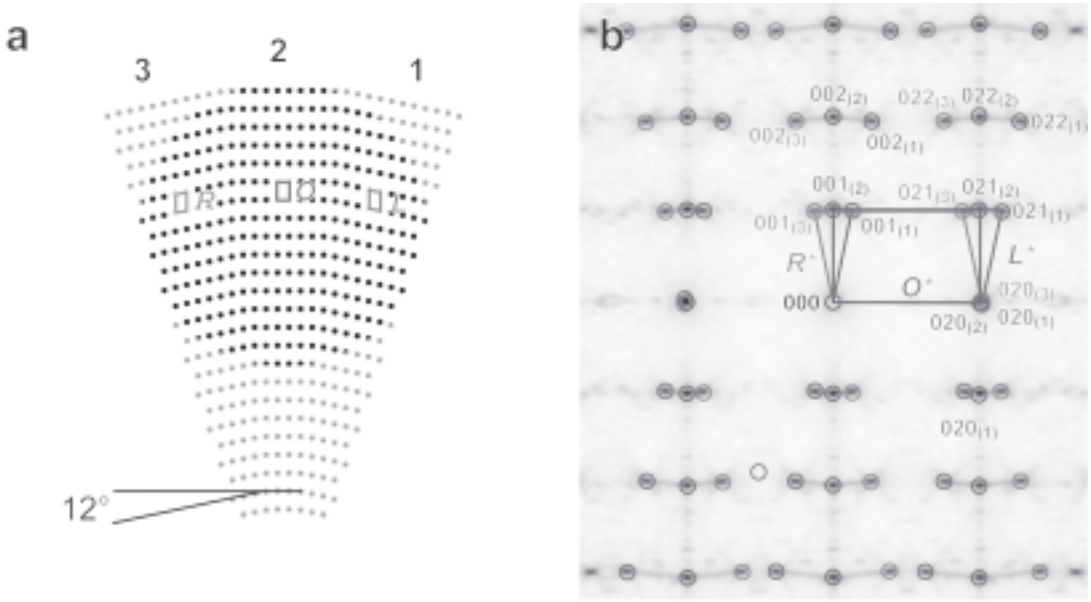

FIG. 8. a) Circular mask of the Bravais lattice nodes of three consecutive sectors of a 30-sector polygonal serpentine along [100]. Note that upon going from sector 1 to sector 3, the sequence of unit cells is *L-O-R* instead of *R-O-L* as for a 15-sector PS (Fig. 7a). b) Corresponding power-spectrum (FFT). Same notations as in Figure 7.

be repeated after three sectors in 15 PS, but after six sectors now in 30 PS. The junction between successive sectors is curved over a few *b*/2 distances while maintaining a constant radius of curvature, as is observed in high-resolution images of PS fibers.

Masks computed according to the above model and the corresponding 2-D Fourier transform are shown in Figures 7 and 8 for a 15-sector and a 30-sector PS, respectively. Radiating series of 00*l* reflections are normal to their three corresponding sectors, and then rotated from each adjacent sector by 24° for 15 PS or 12° for 30 PS.

The [0 2*k l*]* diffraction rows maintain a constant distance of 2*k*/*b* from [00*l*]* in every case, *i.e.*, they are tangential to the frequency rings of radii 2*k*/*b*. However, the distribution of intensity maxima of the power spectrum is not simply a rotated replication of a single sector. Reciprocal nodes undergo a shift along the [0 2*k l*]* row of $-2k\ \alpha/b$ for a rotation of $+\alpha$, due to the above-mentioned shifts. This value corresponds to the length of the circular arc limited by the two contact points of the [0 2*k l*]* row on the 0 2*k* 0 frequency ring.

A prominent peculiarity on the Fourier transform of any of these sets of sectors, for both 15-sector PS and 30-sector PS, is a set of diffuse streaks between basal reflections and a second set of streaks between non-basal reflections (Figs. 7b, 8b).

The streaks between basal reflections are linear segments that link 00*l* reflections of adjoining sectors, on the same frequency ring. This observation is valid for any *l* order of diffraction. As justified in the Appendix, we interpret these streaks as caused by the superimposed curved junctions joining the (001) lattice planes at sector boundaries while keeping a constant radius of curvature along the boundary. Another origin of basal reflection streaks may be the shape factor due to the narrowness and limits of lizardite-like sectors. Since the intersector boundary bisects the angle between the two 00*l* diffraction vectors, Bragg's relaxation of 00*l* reflections will occur along the segment joining 00*l* reflection pairs, *i.e.*, at the precise location of the observed basal reflection streaks. However, linear streaking due to shape factor would overshoot somewhat the two 00*l* spots they link rather than stop right on them. This asterism on 00*l* reflections is visible, although of low intensity, on our FFT simulations, but is never observed in SAED patterns.

The streaks between non-basal reflections are linear segments joining successive 0 2*k l* reflections (Figs. 7b, 8b). All *k* orders of diffraction are involved. These also correspond to the curvature of non-basal lattices planes as they pass through the boundaries between sectors. Any lattice plane parallel to the axis of curvature of the fibril should be curved where the basal plane is curved itself.

Simulations of complete fibers

General features. Figures 9a and b are the lattice-node pattern and the Fourier transform of a fiber of polygonal serpentine with 15 sectors having the simplest orthogonal, one-layer projected stacking as input structure (the projected 1*T*, 1*M*, 2H_1, or 2*Or* polytypes of lizardite, for instance). Diffraction features are reminiscent of those displayed by simulations of chrysotile (Devouard & Baronnet 1995), and will be discussed accordingly.

Compared to chrysotile, successive 00*l* rings are no longer smooth but spotty, with 30 reflections regularly distributed around the ring. This number of 30 reflections is doubled with respect to the number of sectors. This doubling is due to the centering of the Fourier transform completing the acentric 15-fold symmetry of the set of basal planes.

For each *k*, 0 2*k l* reflections are grouped as spotty arcs,"birds in flight", each "bird" having two "wings" of spots connected by diffuse streaks (designated above as non-basal reflection streaks). In other words, the equivalent lattice nodes are situated on evolutes of the concentric circle having 2*k*/*b* as radii. Evolutes of circles are the curves drawn by the trajectory of any fixed point on an infinite straight line "rolling without gliding" on a circle. The cusp point is situated on the circle and the beginning of the two spiral branches resembles the two wings of a bird. See Devouard & Baronnet (1995) for detailed derivation for cylindrical chrysotile.

The continuous shear within the cylindrical structure of chrysotile results in continuous distributions of intensity along the "wings" of such evolutes (Devouard 1995, Devouard & Baronnet 1995). However, in case of polygonal serpentines, these evolutes are marked with distinct diffraction-spots from the non-basal planes of the direct lattice. From a given 0 2 0 diffraction spot, successive diffraction-spots along each wing are due to successive and subtle deviations of the lattice and also to the shortening of the lattice distance where non-basal lattices cut across adjacent sectors (visible in Figs. 9a and 10a if looked at under grazing incidence). The number of "birds" around the 0 2*k* 0 rings is 10 for $k = 1, 20$ for $k = 2$, *etc*., *i.e.*, 10*k* for a one-layer projected stacking. In other words, the curved distance between successive evolutes of any 0 2*k* 0 ring is constant and equal to 1/*t*, which is also the radius of the 001 ring. This is the distance between successive spots along [0 2*k l*]* rows. The axial symmetry of the pattern is ten-fold, as constrained by the set of evolutes of the 0 2 0 ring.

To generate the projected direct lattice of 30-sector polygonal serpentine (Fig. 10a), we retained the model of 1/6 <110> dislocation walls with dislocations present at each interlayer within sector boundaries (Amelinckx *et al*. 1996) rather than the original model of 1/3 <010> dislocations in every other interlayer (Baronnet *et al*. 1994). This choice is validated below, in the Discussion and Conclusions section. For a one-layer polytype constituting a 30-sector PS fiber, the Fourier transform (Fig. 10b) is very similar to the one described above for 15-sector polygonal serpentine in terms of location of diffraction spots (*cf*. Figs. 9b, 10b). Spots are less well defined than for the 15-sector PS because shape-factor effects prevail in the Fourier transform owing to the narrowness of sectors. However, as a main difference between the two cases, each 0 0 *l* and 0 2*k l* spot in the 30-sector case represents two superimposed reflections from opposite sectors. Such doubling comes from the centrosymmetrical distribution of projected lattice-nodes of the 30-sector fiber, so that 0 2*k l* spots systematically overlap 0 $2\bar{k}\ \bar{l}$ spots after half a turn. Again, ten-fold symmetry prevails in projection.

Diffuse streaks connect 0 0 *l* spots along each 0 0 *l* ring as well as 0 2*k l* spots along any branch of the evolutes ("wings") (Figs. 9c, 10c). A major difference between the 15-sector and the 30-sector cases is that streaks are double and connect each successive diffraction-spots for the 30-sector PS, whereas streaks are single and connect every other diffraction spots for the 15-sector PS.

Effects of layer-stacking modes. Having envisaged a greater number of polytypes, we report only on a projected two-layer stacking sequence and on a semi-random ordering of the layers. Figure 11b simulates the power spectrum of a 15-sector PS with a two-layer projected structure (Fig. 11a). The main difference from the one-layer case: there is twice the number of evolutes ("birds") occur around 0 2*k* 0 rings with $k \neq 3n$, whereas for $k = 3n$ (*e.g.*, 0 6 0), the number remains 10*k*. Note that the relative intensity of successive evolutes is modulated, as is the intensity of spots along straight polytype-sensitive rows of a single sector ([0 2 *l*]*, [0 4 *l*]*,...) (*cf*. Fig. 6b). The evolutes thus are geometrically generated through simultaneously "rolling without gliding" the [0 2*k l*]* rows around their respective 0 2*k* 0 frequency rings. Each evolute results from the trajectory of each of the diffraction spots that sits on the [0 2*k l*]* rows with proper reinforcements of intensity due to flat sectors. Accordingly, there are 10*Nk* evolutes around 0 2*k* 0 frequency rings with $k \neq 3n$, with *N* the number of layers in the repeat of the regular polytype. The period and intensity distribution of polytypes in sectors thus may be read by examining round the 0 2*k* 0 frequency ring; the intensity sequence distributed along a 1/*t* length of arc is repeated 10*k* times. The 0 2 0 ring is the best for determining the periodic distribution of intensities of the sector polytypes. It is so because this ring is devoid of any overlap by [0 2*k l*]* rows, $k > 1$. Other 0 2*k* 0, $k > 1$ rings are superimposed on entangled "lateral" reciprocal rows, which prevent the recording of clean profiles of intensity.

Figure 12 is the power spectrum of a semirandom stacking of layers (0, *b*/3 and –*b*/3 shifts in random sequence) in a 15-sector fiber. The 0 0 *l* spots have distributions identical to those of the regular polytypes.

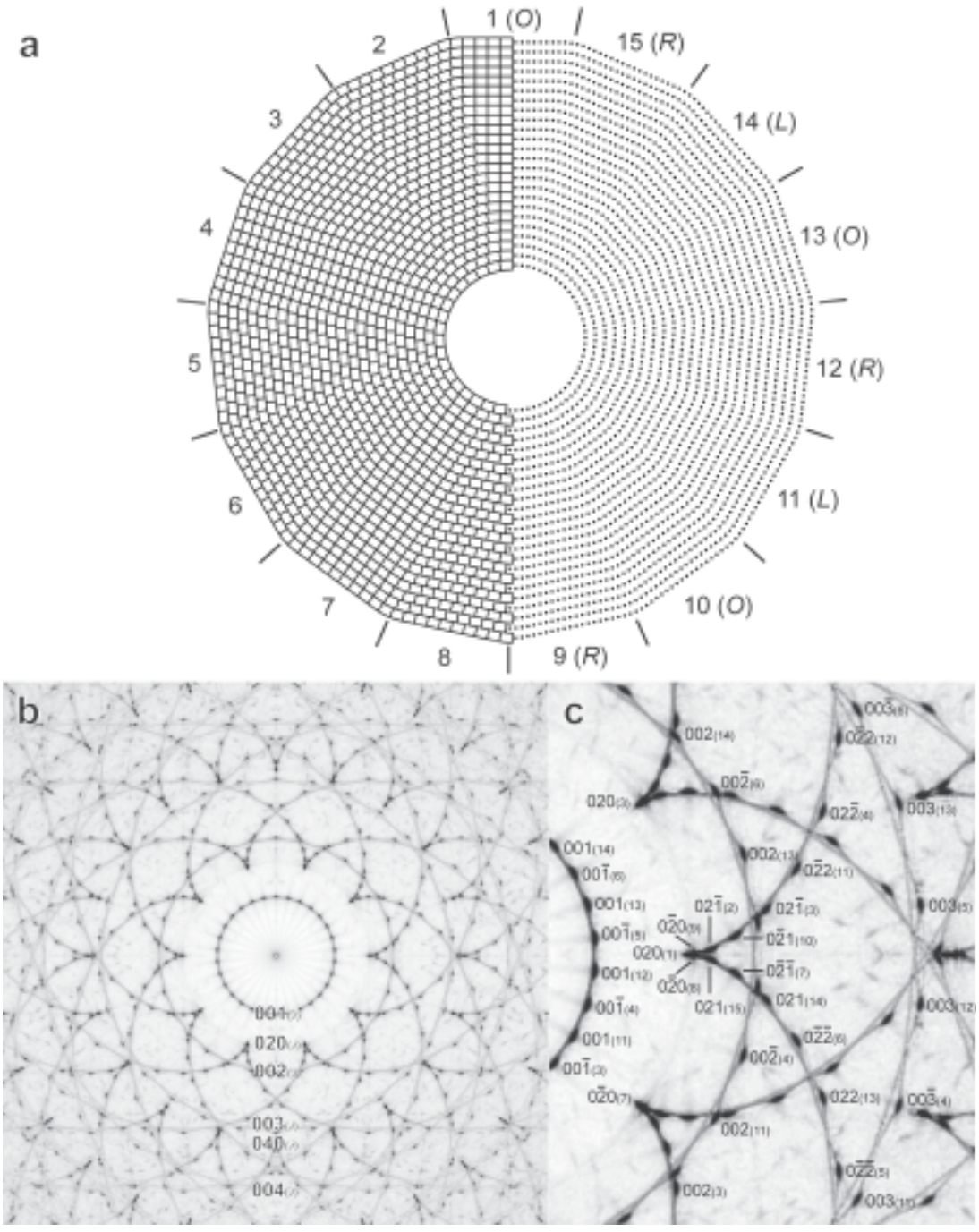

FIG. 9. a) Projected Bravais cells (left half) and lattice nodes (right half) of an entire 15-PS with a ...0, 0, 0, ... projected stacking in the first sector. b) The corresponding power-spectrum with partial indexing as 0 *k l* (*i*), *i* referring to the numbering of sectors. c) Enlarged middle-right part of b) with one of the ten evolutes indexed for low frequencies. Note the diffuse streaks joining every other reflections along diffraction rings and evolutes.

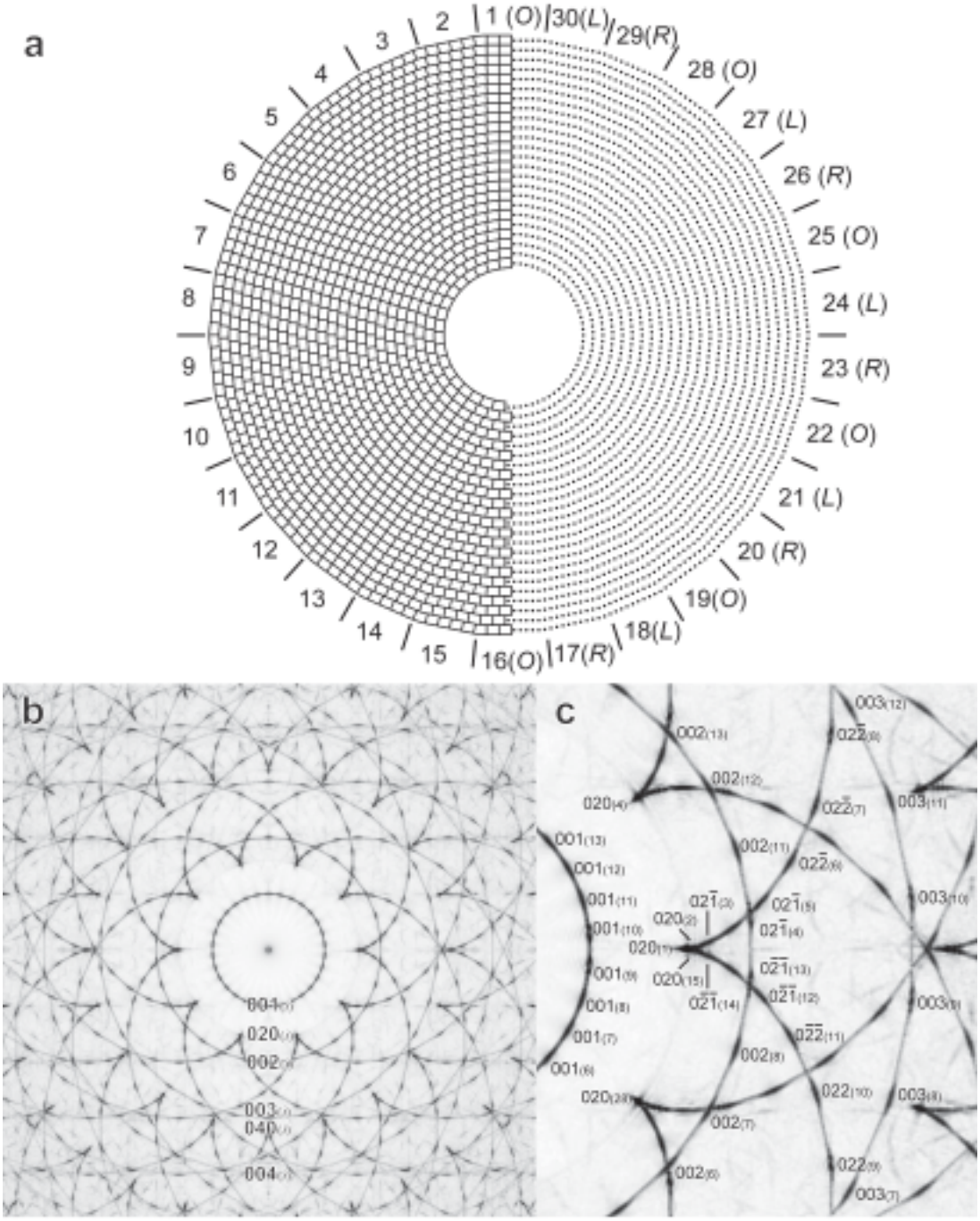

FIG. 10. a) Projected Bravais cells (left half) and lattice nodes (right half) of a 30-sector polygonal serpentine with a ...0, 0, 0, ... projected stacking in the first sector. b) Corresponding power-spectrum with partial indexing. Same notations as in Figure 9. c) Enlarged middle-right part of b) with one of the ten evolutes indexed for low frequencies. Note that diffuse streaks join successive reflections along diffraction rings and evolutes.

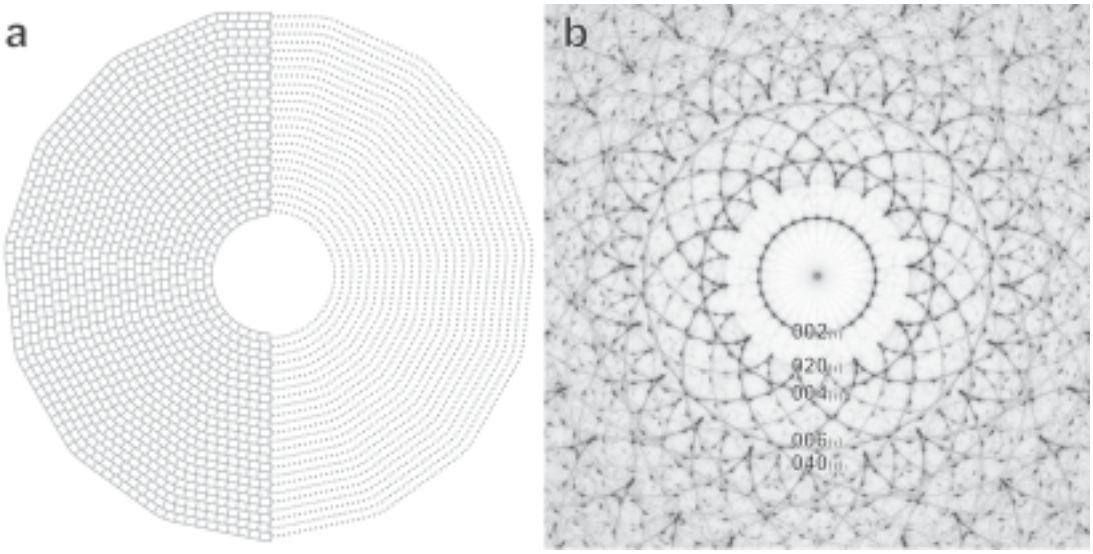

FIG. 11. a) Projected Bravais cells (half left) and lattice nodes (half right) of a 15-sector PS with a two-layer orthogonal stacking (....., +1/3 *b*, - 1/3 *b*, +1/3 *b*, - 1/3 *b*, ...) in the first sector. b) Corresponding power-spectrum with partial indexing. Same notations as in Figure 9. Weak and strong intensities alternate for the twenty inner evolutes, as they do along stacking-sensitive rows in Figure 6b.

However, [0 2*k l*]*, $k \neq 3n$, display continuous streaks. The 0 2 0 frequency ring is almost continuous and marks a limit of space frequency below which there is no diffuse intensity in the background, and above which there is an almost uniform scatter of intensity. Increments of background intensity occur outward in steps beyond each 0 2*k* 0 ring with $k \neq 3n$. For this disordered stacking, scatter may be seen either as the "trace" of the superimposed surfaces swept across by the streaks of [0 2*k l*]*, $k \neq 3n$ when they "roll without glide" around their frequency ring, or as a number of evolutes around a ring that goes to infinity. The 10*k* sharp evolutes still occur around 0 2*k* 0, $k = 3n$ rings.

Whatever the nature of the input polytype and the type of polygonal serpentine (15 or 30 sectors), the following general rules apply. i) Any regular polytype in a sector gives rise to a set of stacking sequences in neighboring sectors that maintains the same repeat as that of the input polytype. This is a direct consequence of the model, and is due to the homogeneous shear of *nb*/3 (15-sector PS) or *nb*/6 (30-sector PS) undergone by all interlayers of the *n*th sector that modifies the stacking sequence without changing the number of layers along the repeat distance. It follows from this "martensite-like" modification of the stacking sequence that any stacking fault in one sector will propagate also as a stacking fault in neighboring sectors. ii) The semirandom stacking introduced in a sector remains semirandom in neighboring sectors owing to the same homogeneous shear.

In summary, the degree of ordered stacking is invariant around a regular polygonal serpentine. Full stacking-order occurs on the diffraction pattern as diffraction curves (evolutes of circles), whereas semirandom stacking occurs as diffraction surfaces. For cylindrical lattices, one dimension is therefore systematically added in the diffraction plane once compared to the case of translational (flat) crystals: in ordered stacking, diffraction spots convert to diffraction curves, and in semirandom stacking, diffraction streaks convert to diffraction surfaces.

The constant relative intensity along "wings" of the evolutes suggests that diffraction intensities of sheared polytypes are not modified, even if their diffraction lattice is slanted. This may be an inherent property of a motif sheared along a plane containing the direction of projection.

Diffuse streaks. The diffuse streaks joining basal and non-basal reflections are now generalized over the whole pattern. They outline 0 0 *l* frequency rings and the "wings" of the evolutes of circles, respectively (*l* being a multiple of the periodicity *N* for regular polytypes).

For 15-sector fibers, streaks between basal reflections are arranged as two interlaced 15-sided polygons, basal streaks connecting every other basal reflection because they correspond to consecutive sectors

(Figs. 9b, c). Accordingly, one polygon of streaks links all successive 0 0 *l* (*i*) reflections such as $l > 0$, and the other polygon does the same for $l < 0$.

In case of 30-sector fibers, basal streaks outline the edges of two 30-sided concentric polygons, the corners of each occurring at the basal reflections 0 0 *l*. This comes from the fact that each reflection is now double, 0 *k l* (*i*) diffraction spots being superimposed onto the 0 (*i* + 15) diffraction spots from the opposite sectors. For the same reasons, each branch of evolute displays two distinct chains of streaked chords (non-basal streaks) for 15-sector fibers, whereas a unique, but doubled, chain of streaks decorates the evolutes of 30-sector PS simulated patterns.

Observed Axial Diffraction-Patterns and Stacking Sequences

Selection of a few contiguous sectors of 15-sector and 30-sector PS

Figures 13 and 14 are the SAED patterns of a few contiguous sectors selected on a 15-sector PS with a dominant two-layer polytype, and on a 30-sector PS with a disordered sequence, respectively. They compare quite well with the main features displayed in Figures 7b and 8b.

The [00*l*]* reciprocal rows are 24° and 12° apart in 15-sector PS and in 30-sector PS, respectively. For both types, linear diffuse streaks connect 00l (*i*) and 00l (*i* + 1) spots, where *i* is the counterclockwise numbering of consecutive sectors ($1 \le i \le 15$ for 15-sector PS, $1 \le i \le 30$ for 30-sector PS).

The [0 2*k l*]* rows of regular polytypes give information about the stacking transformation in going from one sector (*i*) to the next one (*i* + 1). Figure 13 and insets of Figure 4a clearly show how the two-layer unit-cell evolves along successive sectors of a 15-sector PS, in accordance with the imaging and simulation data presented above. An orthogonal (*O*) unit-cell in sector (1) evolves as a unit-cell leaning to the right (*R*) in sector (2), and as one leaning to the left (*L*) in sector (3). Clearly, the unit cells slanting to the left and the unit cells slanting to the right are enantiomorphous images of each other. An ...|*ORL*|*ORLORL*... sequence of unit cells appears along the counterclockwise circuit. In a 30-sector PS with a same two-layer periodicity (insets in Fig. 4b), a first left-leaning unit-cell transforms to a right-leaning one and then to an orthogonal one, *i.e.*, the handedness of the sequence is reversed as ...|*LRO*|*LROLRO*... with respect to the 15-sector case. Note that this reversal is not distinctive, because the handedness actually depends on the stacking periodicity (compare with Figs. 7 and 8, with one-layer polytypes). The **c*** component along the **b*** axis is either +**b***/6 (or –**b***/3), –**b***/6 (or +**b***/3), or zero. In consecutive sectors, the shift pattern is consistent with successive layer-glides of +(1/3)*b* or –(1/6)*b* in direct space, depending on the clockwise or anticlockwise sequence from one sector to the next.

These observations are consistent with *b*/3 and *b*/6 projected shifts between successive layers in crossing sector boundaries for 15-sector and for 30-sector PS, respectively. High-resolution TEM images of 15-sector PS (Fig. 3a) or 30-sector ones (Fig. 3b) confirm these shifts in direct space.

And 15-sector and 30-sector PS fibers as a whole

Though we observe that the global topology of the axial SAED patterns mainly depends on the layer-stacking sequence (see below), any of them could be satisfactorily simulated in the way described above. We report only on selected examples in what follows.

Figures 15 and 16 are examples of [100] axial SAED patterns of a 15-sector PS with a one-layer polytype and a 30-sector PS with a two-layer polytype, respectively. They are very similar to the simulated diffraction-patterns (Fig. 9b for a 15-sector PS, for example). As a major difference between experimental and simulated diffraction-patterns, the basal 0 0 *l* reflections in experimental patterns are more intense than the 0 2*k l* ones. This difference might be the result of neglected structure-factors in our simulations.

Basal reflections. A regular set of 30 radiating rows of sharp 00*l* basal reflections is common to both 15-sector PS and 30-sector PS. Each row is normal to the layering of the flat sectors. Successive orders of reflections 0 0 *N*, 0 0 2*N*, ….., 0 0 *lN* are $(0.73\ \text{nm})^{-1}$ apart, *N* being the polytype periodicity. Thirty equispaced reflections with the same order of diffraction *l* sit on concentric rings. Counterclockwise numbering *i* of the successive sectors in direct space allows indexing of basal reflections as 0 0 *lN*(*i*). Positive values of *l* are taken toward the rim of the corresponding sector.

Accordingly, in a 15-sector PS, successive half-rows index as: 0 0 *lN* (1), 0 0 *l* (8), 0 0 *lN* (2), 0 0 *l* (9), 0 0 *lN* (3), 0 0 *l* (10), *etc*., *i.e.*, ...0 0 *lN* (*i*), 0 0 *l* (*I* + 7), ... with *l, N* and $1 \le I \le 8$ taken as positive integers. The above alternation comes from the acentric setting of flat layers around the axis of any fiber with an odd number of sectors.

For a 30-sector PS, there is an intrinsic overlap of the 0 0 *lN* basal reflections of one sector by the 0 0 *l* ones from the antiparallel sector. This is due to the inherent centering of the configuration of an even number of sectors. The pairs of reflections are: 0 0 *lN* (1) + 0 0 *l* (16), 0 0 *lN* (2) + 0 0 *l* (17), 0 0 *lN* (3) + 0 0 *l* (18), *etc*., *i.e.*, ... 0 0 *lN* (*i*) + 0 0 *l* (*i* + 15)... with *l, N* and $1 \le I \le 15$ as positive integers. In this case, each basal diffraction-spot is doubled, and their match is usually impressive, which indicates a strict crystallographic control upon the sectorial arrangement.

A few cases of 30-sector PS displaying radial splitting of 0 0 *lN* reflections, while keeping a constant-split distance for any *l,* has been tentatively explained by

electron optical refraction phenomena (Amelinckx *et al.* 1996, their Fig. 4). Also, occasional faint spots have been observed that halve the **c*** distance. These cannot easily be attributed to non-extinct forbidden reflections caused by conditions of dynamic diffraction operating on a even-layered polytype. In some cases, alternation of two types of layers (ordered mixed-layering) or of two arrangements (polar *versus* antipolar?) of a unique type of serpentine layers thus may be possible within sectors.

Non-basal reflections. In both types of fibers, there are thirty [0 2*k l*]* (*i*) rows tangent to each of the successive orders *k* of any 0 2*k* 0 [*i.e.*, ($k \times 0.45$ nm)$^{-1}$] space frequency-ring, and they run parallel to successive [00*l*]* (*i*) rows (*e.g.*, Fig. 17). In the diffraction plane, they form nested semi-infinite coronae having each one of the 0 2*k* 0 space frequency-rings as inner diameter and going to infinity outward. In 15-sector PS, each [0 2*k l*]* row comes from a single sector. The [0 2*k l*]* (*i*) and [0 $\bar{k}$ *l*]* (*i* + 15) rows overlap systemati-

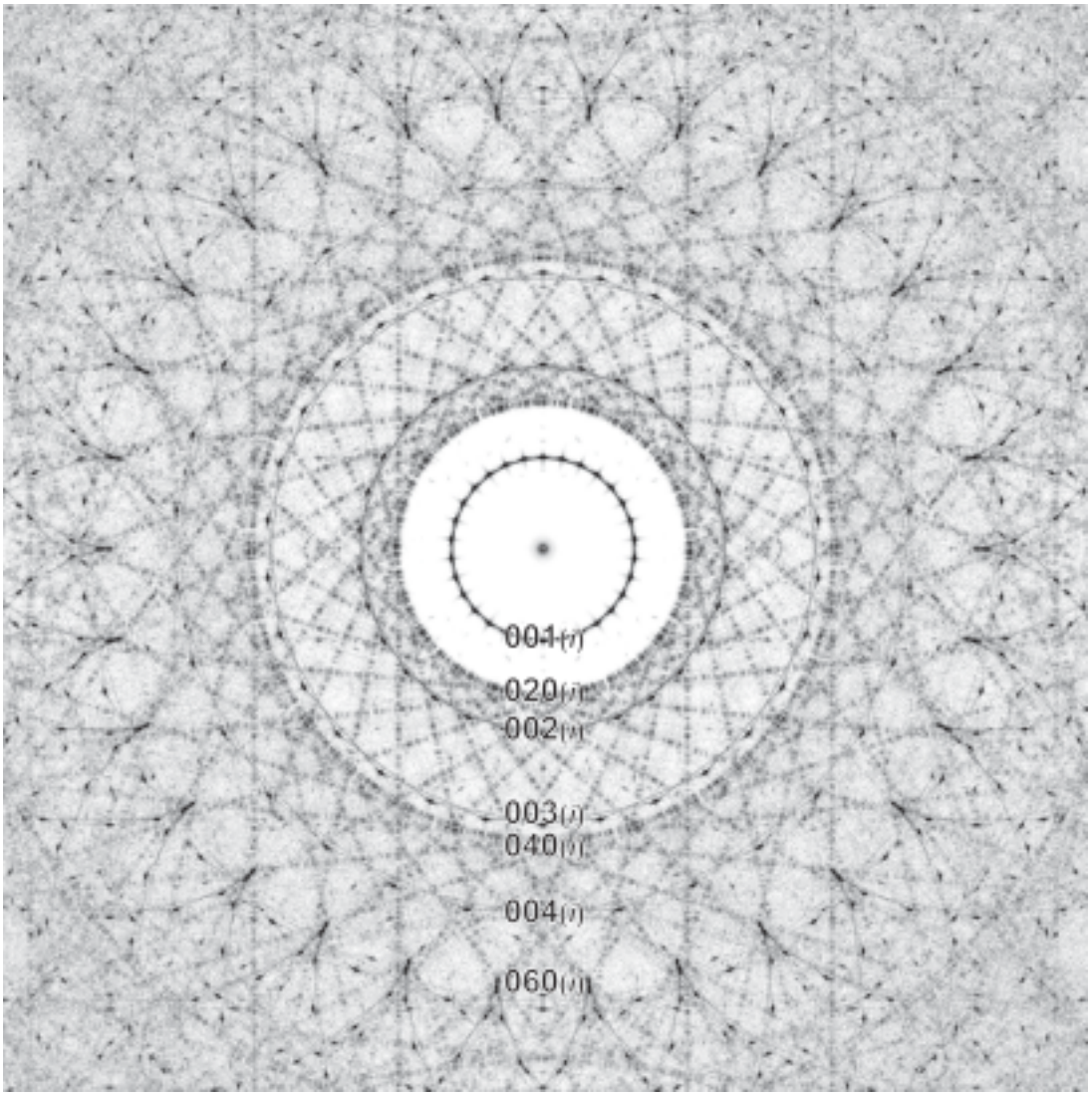

FIG. 12. Lattice Fourier transform of a 15-PS with a 2-D semirandom stacking of layers (*i.e.*, combining randomly 0, +1/3 *b,* and -1/3 *b* shifts) in one sector. Only frequency rings are indexed. -: undefined *l*. Note the diffuse intensity increasing by steps in the background, beyond the 0 2 0 (*i*) and 0 4 0 (*i*) rings.

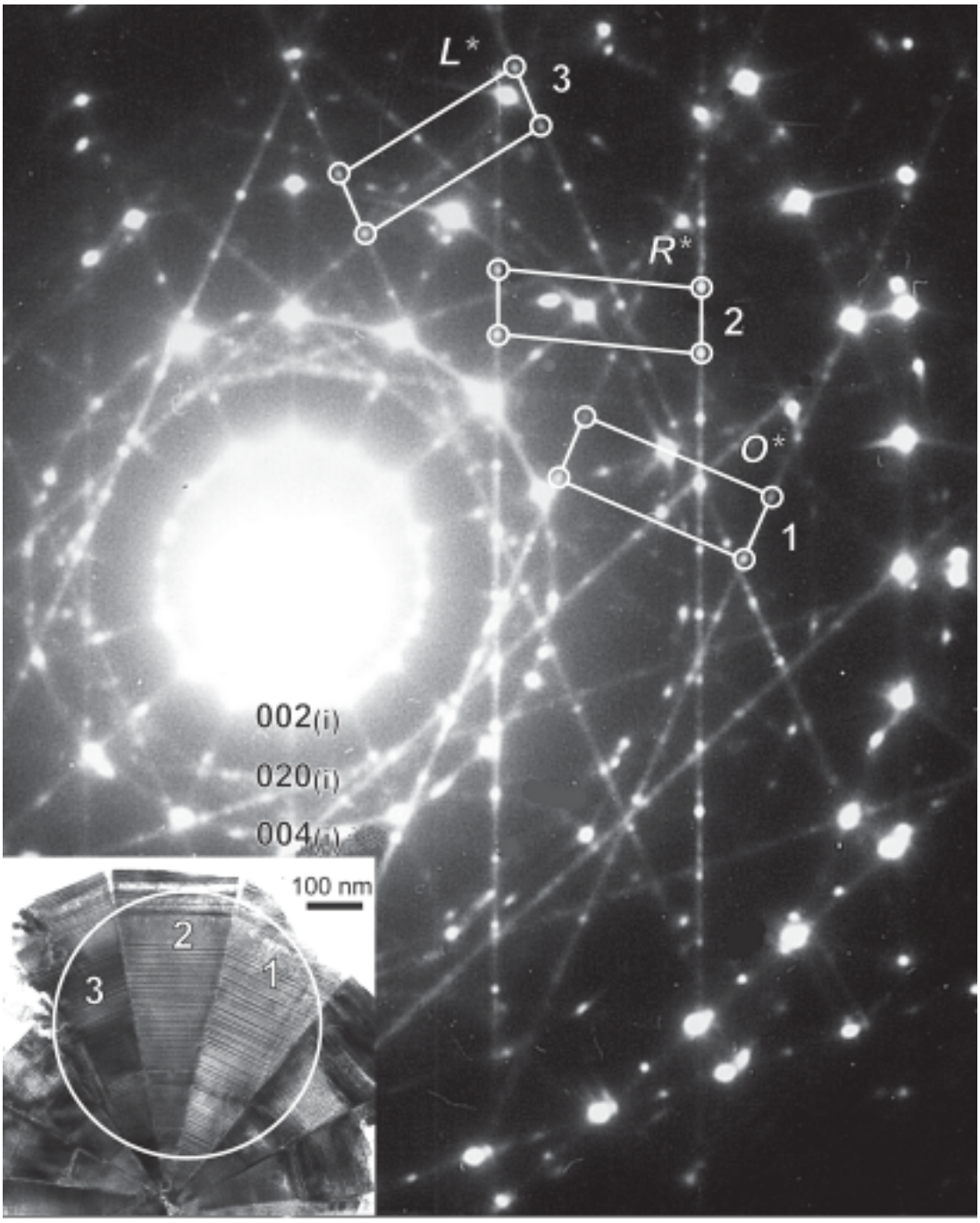

FIG. 13. Electron-diffraction pattern of four contiguous sectors from a 15-sector polygonal serpentine displaying mostly two-layer 2D-stacking with some disorder. Reciprocal unit-cells *O**, *R**, and *L** correspond to the *O*, *R*, and *L* direct unit-cells in sectors 1, 2, and 3, respectively. Inset: image of the corresponding fiber with location of the selection aperture (white circle) used to record the SAED pattern.

cally in a 30-sector PS. Assuming total structural continuity around the fiber, the total shear undergone between successive layers in going from sector (*i*) to sector (*i* + 15) would be $\pi t \approx 5b/2$ (Baronnet *et al*. 1994), *i.e.*, the projected stacking sequences are the same but turned by π on the fiber axis. Consequently, the diffraction patterns might be presumably centered if Friedel's Law is valid so that opposed sectors will be identical and might therefore duplicate the same information about their stacking sequences. Both sequences look identical in [100] projection, but differ in 3-D space as the total interlayer shift, $5b/2$, is not an integral multiple of *b*.

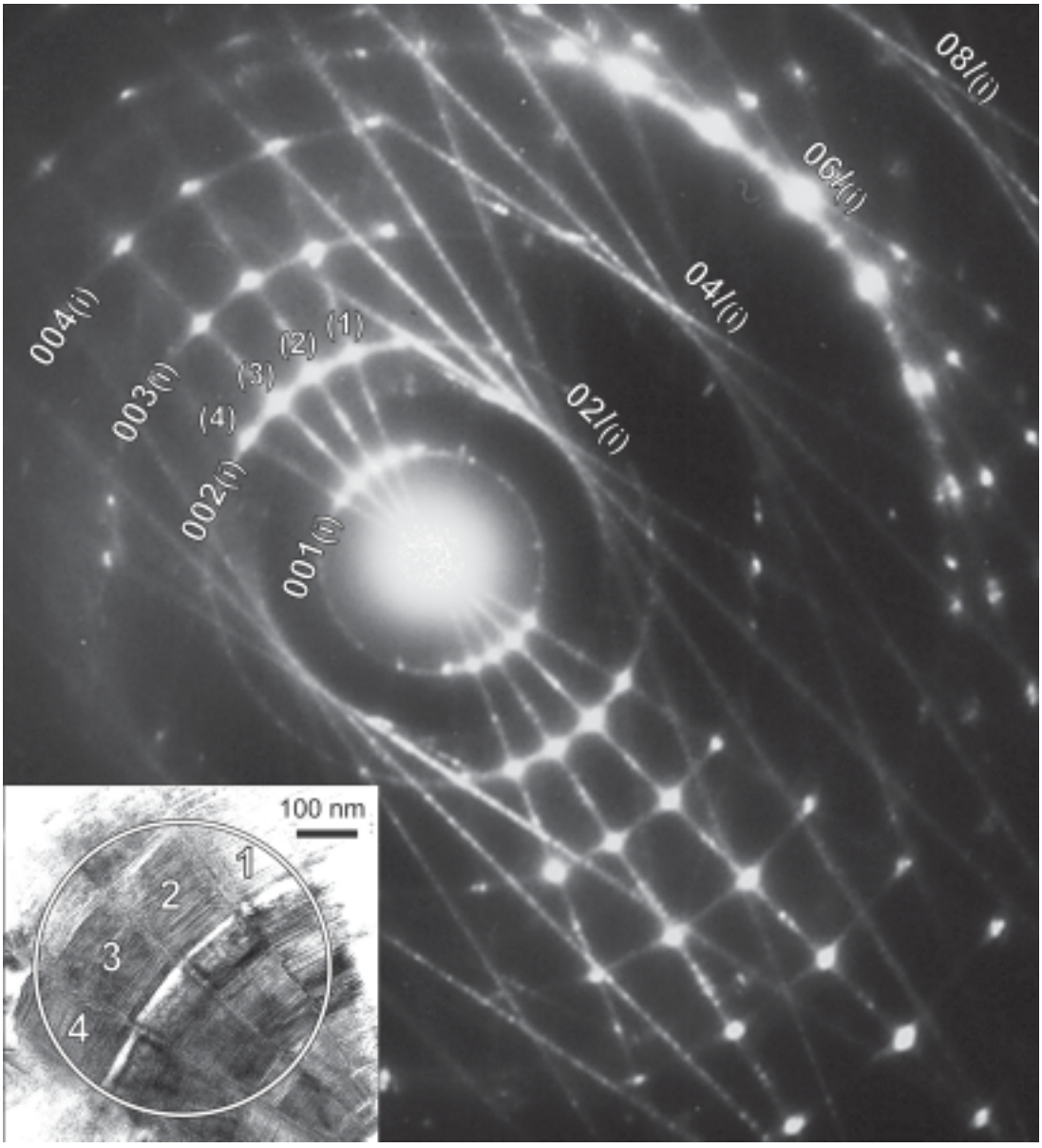

FIG. 14. Electron-diffraction pattern of a few contiguous sectors from a 30-sector polygonal serpentine exhibiting 2D semirandom stacking. Streaks are almost continuous along [0 ± 2 *l*]* and [0 ± 4 *l*]* rows. Same comment as for Figure13 regarding the additional reflections along [0 0 *l*]* and [0 ± 6 *l*]* rows.

Modifications in layer-stacking within individual sectors. The [0 2 *l*]*, [0 4 *l*]*, [0 8 *l*]*, [0 10 *l*]*, *i.e.*, [0 2*k l*]* rows with $2k \neq 0$ mod 6 have variable intensity-profiles, including sharp, equispaced spots of regular polytypes, complex admixtures of the former, or even continuous streaking of intensity. Periodic or non-periodic projections are recorded in TEM images. A periodic projection may mean either a periodic (regular) polytype or an aperiodic stacking sequence depending on the unknown pattern of order of layer-stacking components along [100]. Most common periodic projections of polytypes are two-layered (Figs. 4a, b, 13 and 16), four-layered (Figs. 3a, 17), and six-layered (Fig. 18) sequences, as also noted elsewhere [Jiang & Liu (1984), and Dodony's (1988) data reported by Papp (1990)]. This statement holds for both 15-sector PS and 30-sector PS. The actual sequence of intensity is commonly less clear for the latter because of the overlap of diffraction rows produced by opposite sectors. Better visibility of the intensity profile (and of the sequence of

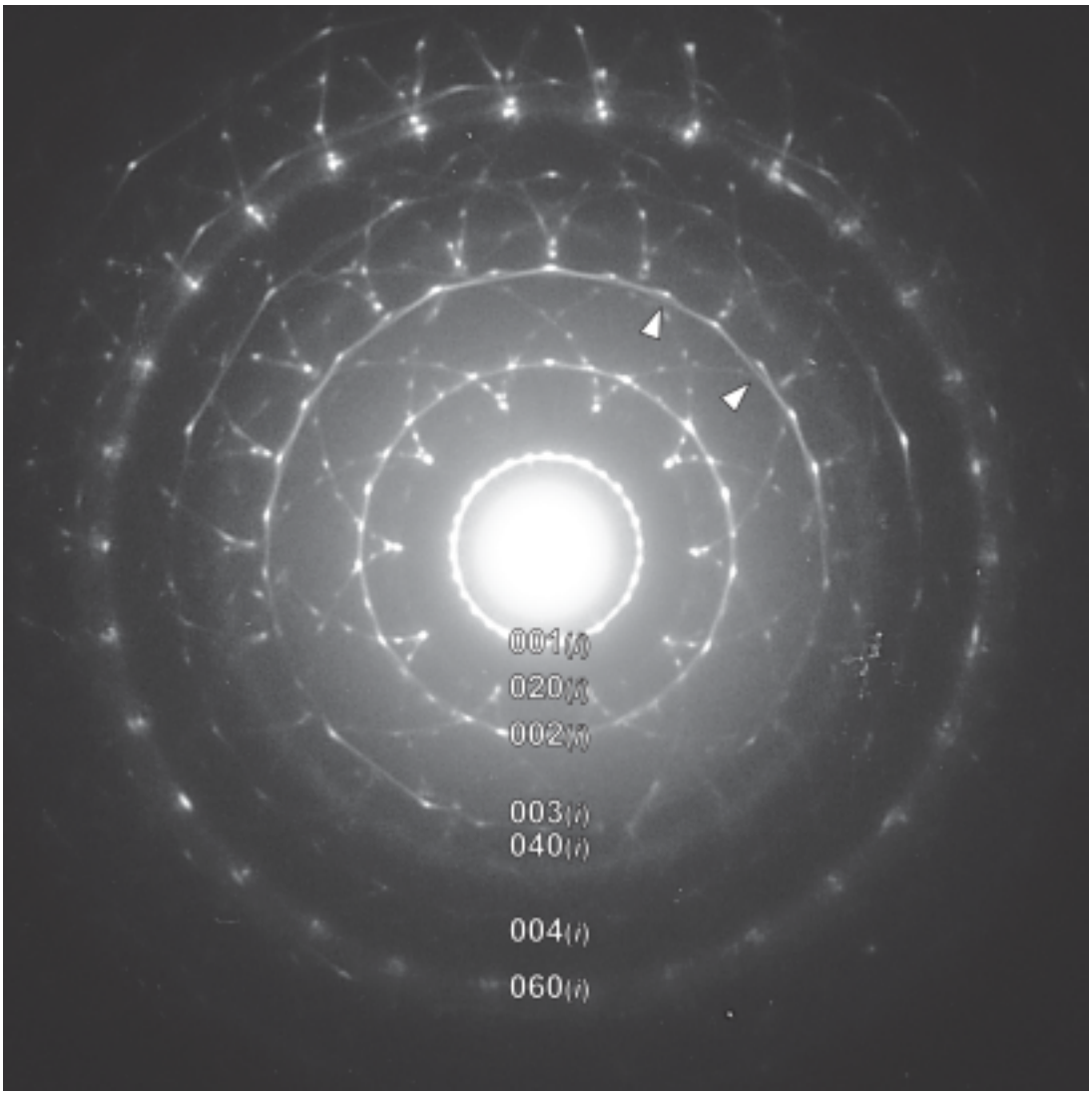

FIG. 15. A [100] zone-axis SAED pattern of a regular 15-sector PS with a one-layer polytype. The selection aperture was centered on the fiber axis. The ten-fold symmetry of the pattern as a whole arises from a true five-fold symmetry of the fiber (see text).

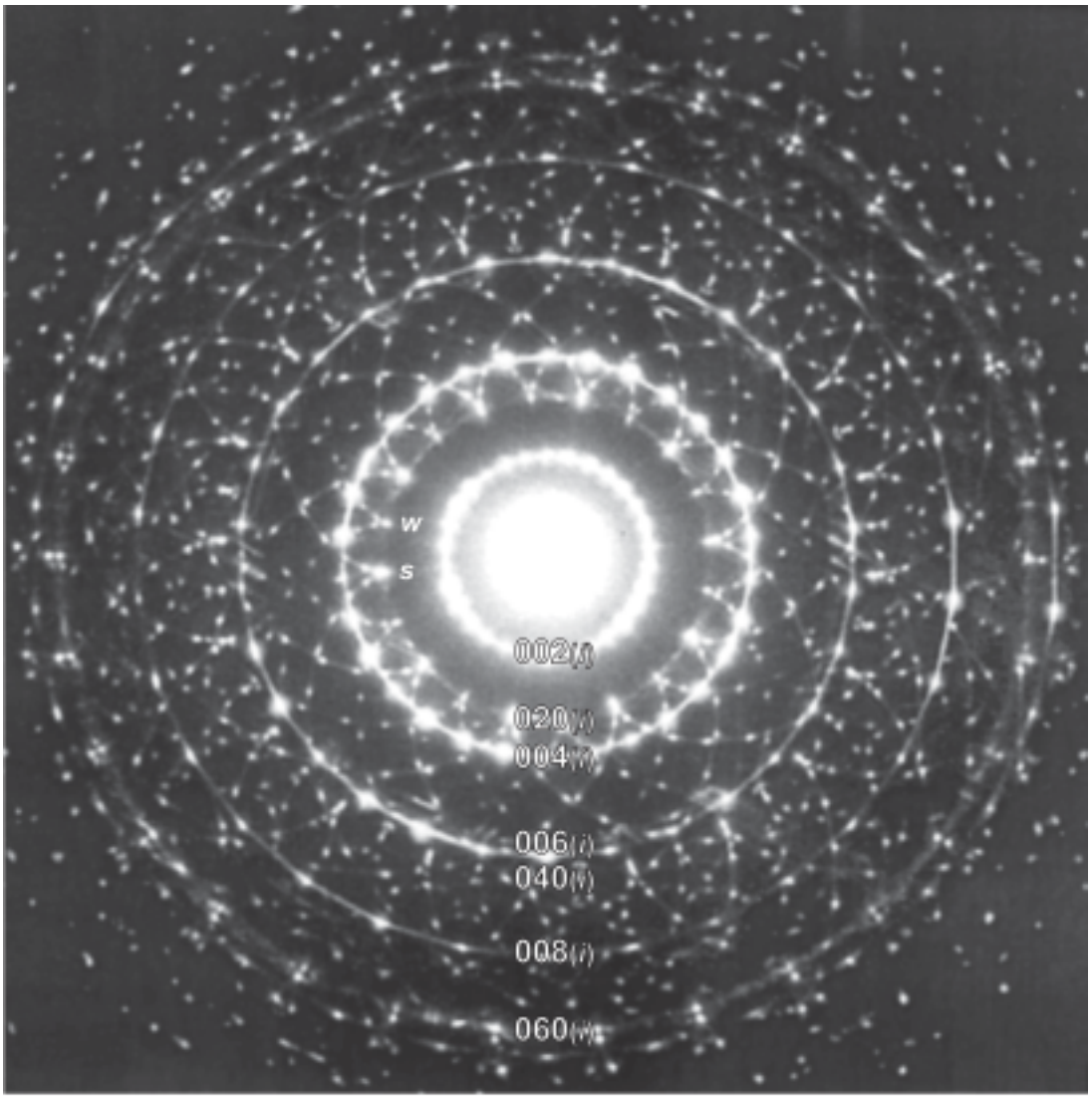

FIG. 16. A [100] zone-axis SAED pattern of a 30-sector PS with a two-layer polytype. Note the alternation of strong (s) and weak (w) "birds" around the 0 2 0 frequency ring, lowering the projected symmetry to ten-fold, and the propensity of smeared reflections to merge with connected streaks similar to the simulation in Figure 10.

direct-space contrast) is obtained by tilting the fibers slightly off their axis (inset in Fig. 18): more intensity passes through a smaller number of characteristic rows, and superperiodicity spots are rendered more visible by enhanced conditions of dynamic diffraction. We notice also how such a tilt emphasizes the imprint of the periodic distribution of intensity in the polytype on the 0 2 0 frequency arc. The usual thick-on-average sections (>20 to 50 nm) of PS fibers and resulting dynamic conditions prevent serious comparisons with the simulated profiles of intensity for lizardite reported by Bailey & Banfield (1995) under kinematic conditions. Also 30-sector PS fibers with semirandom sequences of stacking are quite common (Fig. 19). Note how this SAED pattern resembles the simulated pattern of a 15-sector PS with the same stacking sequence (Fig. 12).

Diffuse streaks. Diffraction streaks as segments or arcs connecting reflections from different sectors are ubiquitous features on the axial electron-diffraction pattern of any single fiber (Figs. 15, 16, 18 and 19). These

streaks, usually rectilinear, connect sharp reflections two by two as interspot segments that do not extend beyond linked reflections.

In case of 15-sector PS, streaks between basal reflections link every other 0 0 *l* reflections (Fig. 15), whereas in the case of 30-sector fibers, they connect all successive 0 0 *l* (*i*) reflections (Fig. 19). That these streaks are chords, on any 0 0 *l* frequency-ring, is particularly visible in Figures 15 and 16 if one looks at them along a line of grazing incidence. However, if a cylindrical core of chrysotile occupies the center of the polygonal fiber, these streaks are no longer chords but arcs, or a mixture of chords and arcs. Such arcs underline the frequency ring (Fig. 18). This is consistent with a Debye–Scherrer ring, itself typical of a constant basal distance between curved layers. Their radius of curvature thus is increased (or decreased) by the constant layer-spacing when moving from one layer to the next one. This is a basic property of chrysotile tubes.

Despite the great resemblance of the SAED patterns of both types of PS fibers, the arrangement of basal streaks is diagnostic for their recognition as 15-sector or 30-sector PS in the absence of any direct-space image.

Diffuse streaks also are present as linear segments joining non-basal reflections sitting on the same branch

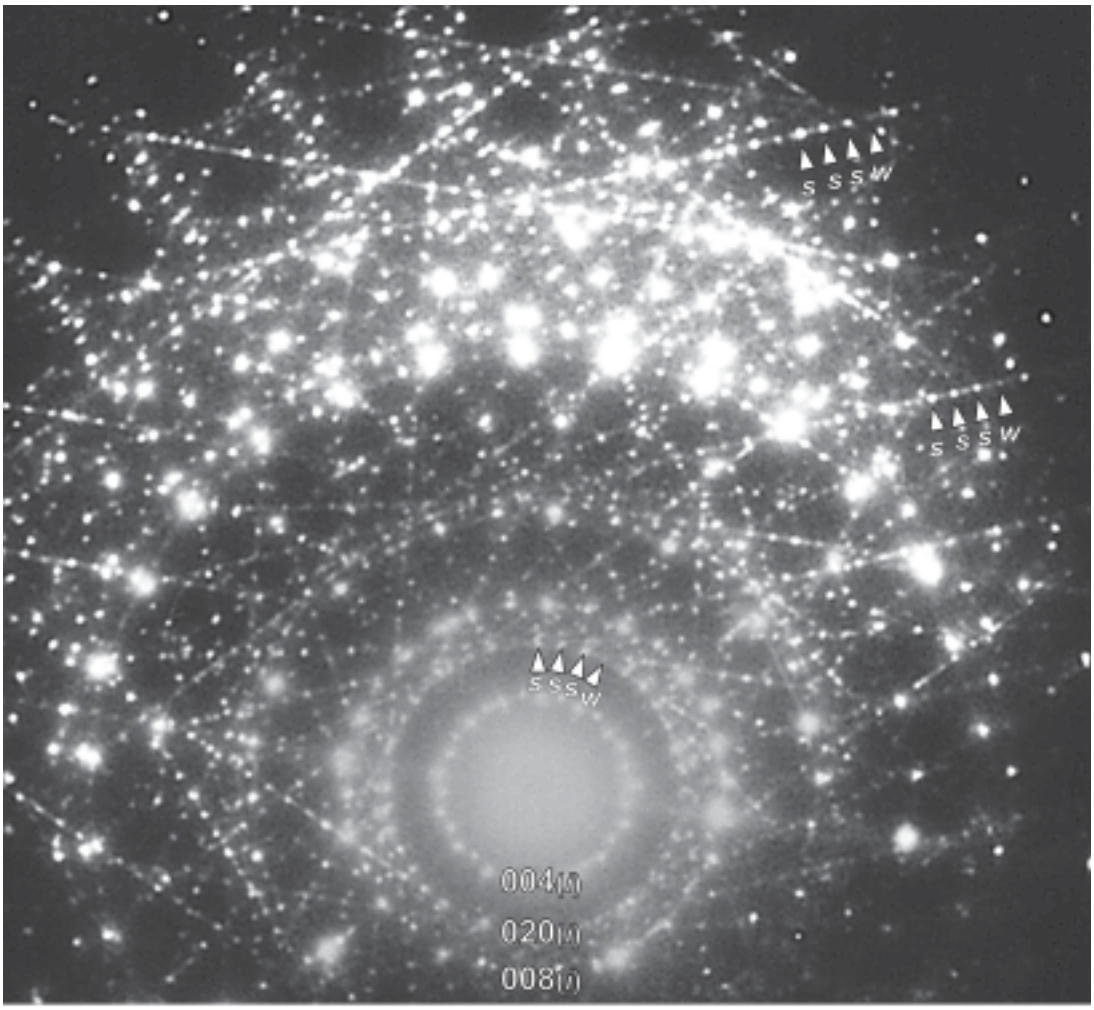

FIG. 17. A [100] zone-axis SAED pattern of a 15-sector PS with a four-layer stacking sequence, *i.e.*, a non-standard (long-repeat or complex) polytype. The intensity sequence strong, strong, strong, weak (sssw) shows up along non-basal diffraction rows (white arrowheads) and along the 0 2 *l* frequency ring as well (black-and-white arrowheads).

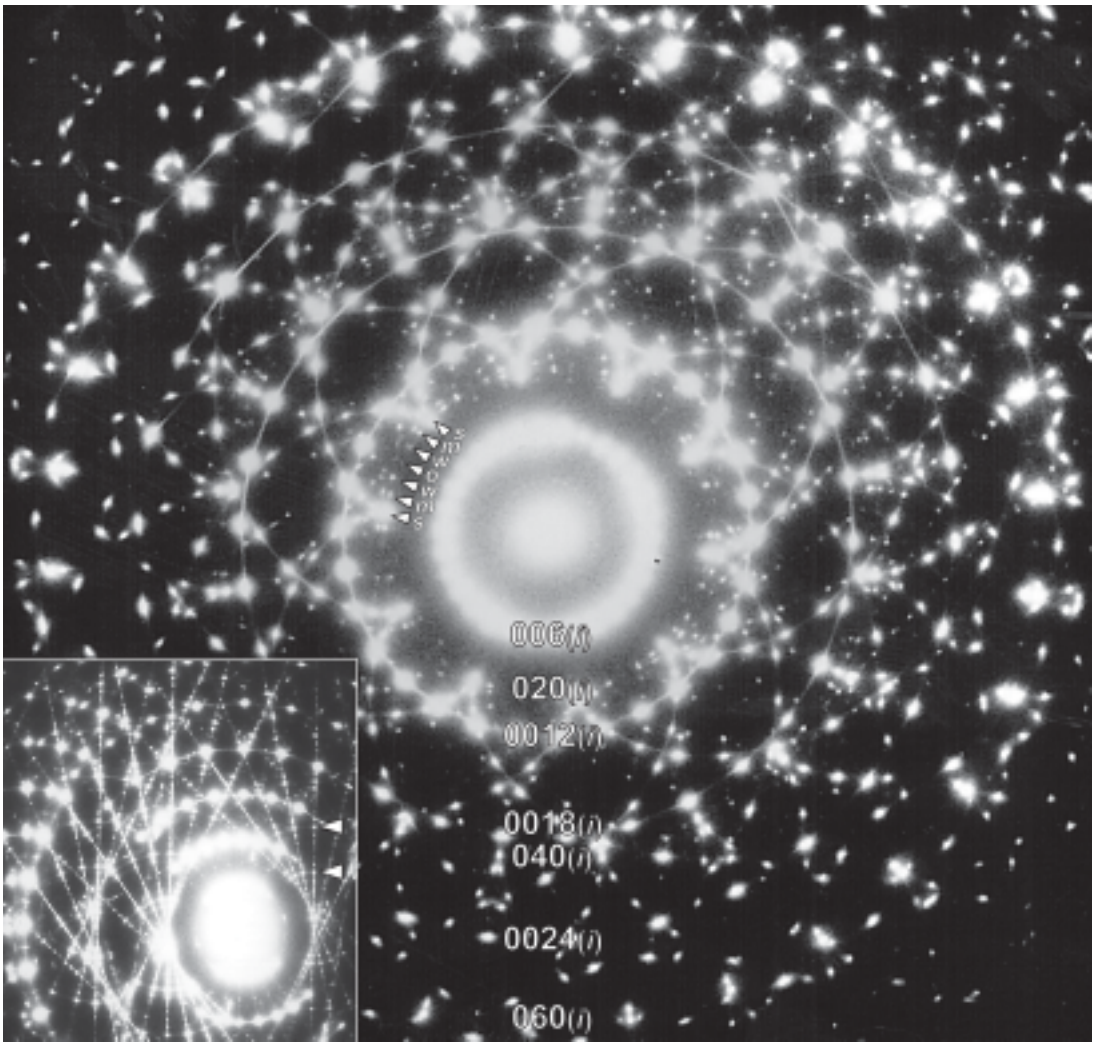

FIG. 18. A [100] zone-axis SAED pattern of a 30-sector PS with a six-layer stacking sequence. Note the almost perfect tenfold 2D symmetry of the pattern. The intensity distribution strong, medium, weak, nil, weak, medium (*smw0wm*) along the 0 2 0 frequency ring is marked by arrows. This is hardly recordable elsewhere because too many reflections overlap. Note that incorrect exposure would have led to misinterpretation of this pattern as a one-layer stacking sequence similar to that in Figure 15 or to the one reported by Dodony (1997a, his Fig. 1). Inset: the same fiber after a slight tilt around a nearly vertical axis. Now intensity sequences along rows of non-basal reflection may be easily recorded (*e.g.,* between the two white arrowheads).

of any evolute of a 0 2*k* 0 frequency-ring. They may be visible in the case of a short-period, well-ordered polytype, where sharp spots are observed (Figs. 15, 16), or less visible in the case of semirandom stacking, where only evolutes on 0 6 0 (more generally 0 2*k* 0, $k = 3n$) are distinctly streaked (Fig. 19). Branches of evolutes also display interlaced (15-sector PS) or single (30-sector PS) chains of streaks, although the fact that such a chain might be actually made of two overlapping chains is usually hard to see.

DISCUSSION AND CONCLUSIONS

Previous investigators considered polygonal serpentine as an exotic and uncommon modification of chrysotile (Cressey 1979, Cressey & Zussman 1976, Middleton & Whittaker 1976), somewhat intermediate in microstructure between the rolled chrysotile and the flat lizardite. However, it turns out that most veins in serpentinites from the Western Alps contain PS in various amounts when looked at carefully with the trans-

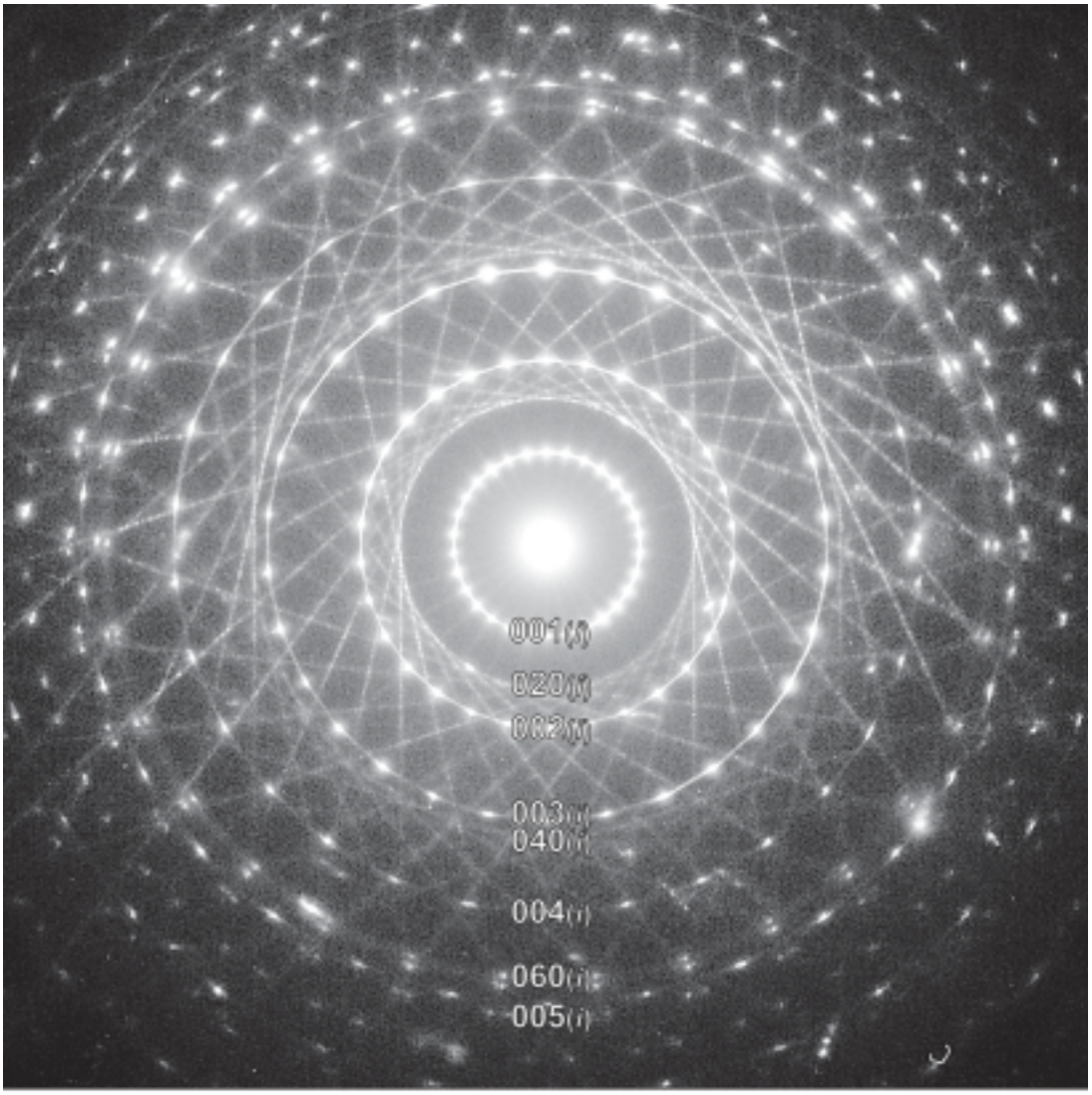

FIG. 19. A [100] zone-axis SAED pattern of a 30-sector PS with a disordered (semirandom) layer stacking. This pattern is from the fiber shown in Figure 2. Note that the 0 2 *l* streaks roll around the 0 2 0 frequency ring, which is a continuous circle with a constant intensity.

mission electron microscope (Belluso *et al.* 1998). In agreement with Papp (1988, 1990), both natural (Yada & Liu 1987) and synthetic (Devouard *et al.* 1997) "chrysotile fibers" larger than *ca.* 100 nm in diameter turn out to be PS. Nearly all such fibers display 15 or 30 radially distributed sectors of flat serpentine (Chisholm 1992, Mitchell & Putnis 1988, Yada & Liu 1987), but exceptionally 29 sectors were also observed, as well as more than forty (Devouard 1995). The reason(s) for the occurrence of such fixed numbers of sectors inspired various crystallographic models (Chisholm 1991, 1992, Dodony 1993, 1997a) and dislocation-based models (Baronnet *et al.* 1994, Amelinckx *et al.* 1996) .

Microstructural model of polygonal serpentines

The place of polygonal serpentines among other varieties of serpentine depends strongly on the state of knowledge of the intimate microstructure of these fibers, and of the models proposed. Chisholm (1991,

1992) assumed a unique stacking structure of the flat layers inside all sectors of one and the same fiber. Furthermore, "kink" angles formed by (001) lattice planes at sector boundaries are assumed to be controlled by addition of integral numbers of octahedra at the border of flat sectors. According to Chisholm's model, 15- and 30-sector PS appear as cyclic twins on the lizardite structure with sharp but corrugated contact-twin planes (sector boundaries). As deduced by Devouard (1995) and Dodony (1997a), a thirty-fold symmetry of the axial diffraction-pattern of the 30-sector PS would result from Chisholm's model, but this is contrary to Dodony's and our observations.

Dodony (1993, 1997a) suggested that 30-sector fibers could be made of flat layers of lizardite changing their polarity at sharp intersector boundaries. He claimed that this model is supported by simulated and observed TEM contrasts of sectors in natural fibers. His model, however, cannot be reconciled with 15-sector fibers since they would present an odd number of polarity reversals. Following Dodony's model, 30-sector PS could be interpreted as a sort of polygonal roll of "para-antigorite" with zero amplitude of the modulation waves. Para-antigorite is mentioned because in Dodony's model, the 1:1 layers would be modulated along the *y* axis, not along the *x* axis as in normal antigorite.

Baronnet *et al.* (1994) hypothesized that sector boundaries could be seen as partial dislocation-walls. The continuity of the single-layer structure, including layer polarity, would be maintained at crossing of sector boundaries. The stacking sequences of serpentine layers in successive sectors would be related topologically by martensite-type shears.

Our combined use of conventional and high-resolution TEM imaging, electron-diffraction data, and the numerical simulation of diffraction patterns sheds some new light on the intimate microstructure of polygonal serpentines. Structural continuity and homogeneous shearing of the stacking sequences from one sector to the next are unambiguously demonstrated in both 15- and 30-sector PS fibers by high-resolution images, and by the SAED patterns.

A most important contribution is the determination of the ubiquitous curvature of serpentine layers at sector boundaries, for both 15- and 30-sector PS. Such curvature has been overlooked by former microscopists, probably because a very precise alignment of the zone axis is needed to produce a consistent image around the entire fiber. Without the precise alignment, a seemingly sharp boundary and out-of-phase positions of the (00*N*) lattice fringes are observed, which suggests structural disruption of the structural continuity across sector boundaries. Different off-axis positions of successive sector-structures likely cause phase shifts of the images of the two neighboring sectors (Guthrie & Veblen 1990). Diffraction streaks interpreted here as signatures of such curvatures may be found also in all the axial SAED patterns of 30-sector PS published by Dodony (1997a; his Figs. 1a, 4a, 6, 8). In the absence of high-resolution images of the boundaries, he provided no explanation of these streaks in diffraction space. Instead, Dodony proposed sharp boundaries made of 1:1 layer polarity reversals plus a 12° tilt of the basal planes on the fiber axis. Accordingly, the same polarity of layers would be found in every other sector. The present work does not confirm his model, even if very exceptional 30-sector fibers with modulated lizardite layers can be found (Devouard & Baronnet, in prep.). In the latter case, modulation contrasts occur inside the sectors and are aligned normal to the layer traces, not along the boundary. In addition, a numerical Fourier transform of Dodony's model (Fig. 20) displays 0 0 *l* intensities that are markedly different from those of experimental SAED patterns and from our simulated patterns as well. This difference probably comes from the fact that Dodony's power spectrum is generated from the FT of a direct-space model (his Fig. 11) that includes details of the structure within the serpentine layer (triangles for tetrahedra, dots for oxygen atoms…), thus inducing strong differences in intensities (structure factors) for successive 0 0 *l* and 0 2*k l* frequency rings. These differences in intensities, as well as the difference in resolution of Dodony's and our simulations, make the comparison of both models on the basis of the simulated patterns very difficult. In addition, the boundary reversal proposed by Dodony cannot occur in 15-sector PS, as the model would systematically leave two contiguous sectors with the same polarity because of the odd number of sectors. No such unique boundary in 15-sector PS has been observed in our images.

Our work demonstrates that all HRTEM and SAED observations of both 15- and 30-sector PS fibers are consistent with the dislocation model proposed by Baronnet *et al.* (1994). However, Baronnet *et al.* (1994) favored an elastic model for 30-sector PS according to which a 15-sector PS would convert to a 30-sector one beyond a certain diameter of fiber. This conversion would occur through elastic interaction between dislocations of the 15 walls, making any other dislocation of each wall form 15 new walls in between. Hence dislocations of a unique type 1/3 [010] were proposed for both types of fibers. This would result in a *b*/3 shear (homogeneous) of all interlayer spaces for a 15-sector PS, and the same shear, but between every other interlayer space for a 30-sector PS. This model is not consistent with the homogeneous shear of 30-sector fibers indicated by HRTEM (*e.g.*, Fig. 3b). It is also not consistent with the modifications of stacking sequences in the 30-sectors PS (Fig. 16), or with contiguous one-layer polytypes in a 30-sector PS, as observed by Dodony (1997a, his Fig. 1a). Instead, the observations support the possibility of distinct dislocations for 15-sector PS (1/3 [010]) and 30-sector PS (1/6 <110>), which also was considered (Baronnet *et al.* 1994, Amelinckx *et al.* 1996), but not developed in terms of

polytype generation in sectors. Two other arguments also noticeably weaken our formerly proposed mechanism of splitting of dislocation walls controlled by size. i) The 30-sector PS are *statistically,* but not *systematically*, larger than 15-sector PS in a given serpentinite; ii) the proportion of each PS type responds to the geological occurrences (Belluso & Baronnet, unpubl. data).

Invoking 1/6 <110> partial dislocations for 30-sector fibers (or any other system of dislocations projecting as *b*/6 along the [100] zone) implies that the fibers must be subjected to some strain at sector boundaries, as these dislocations have a component *along* the fiber axis (Amelinckx *et al*. 1996). This axial stress may be (at least partly) releaved by non-cylindrical, *i.e.*, helical or conical, wrapping of the layers. Dodony (1997a) interpreted a chiral wrapping from the fading of non-basal reflections in axial SAED patterns. This effect may also originate from a semirandom stacking of the PS layers, as indicated by Figures 12 and 19. On the other hand, in using the diffraction mode to finalize the alignment of [100] SAED patterns of PS fibers, we generally observe that a perfectly intensity-symmetrical SAED pattern is rarely obtained. Instead, the region of most excited reflections rotates on the transmitted beam. This behavior suggests that the global zero-order Laue zone of polygonal fibers may be somewhat conical instead of being perfectly flat. The zone axes of individual sectors are commonly not strictly colinear, but presumably arranged as the generated lines of an acute cone centered on the fiber axis. This interpretation is further supported

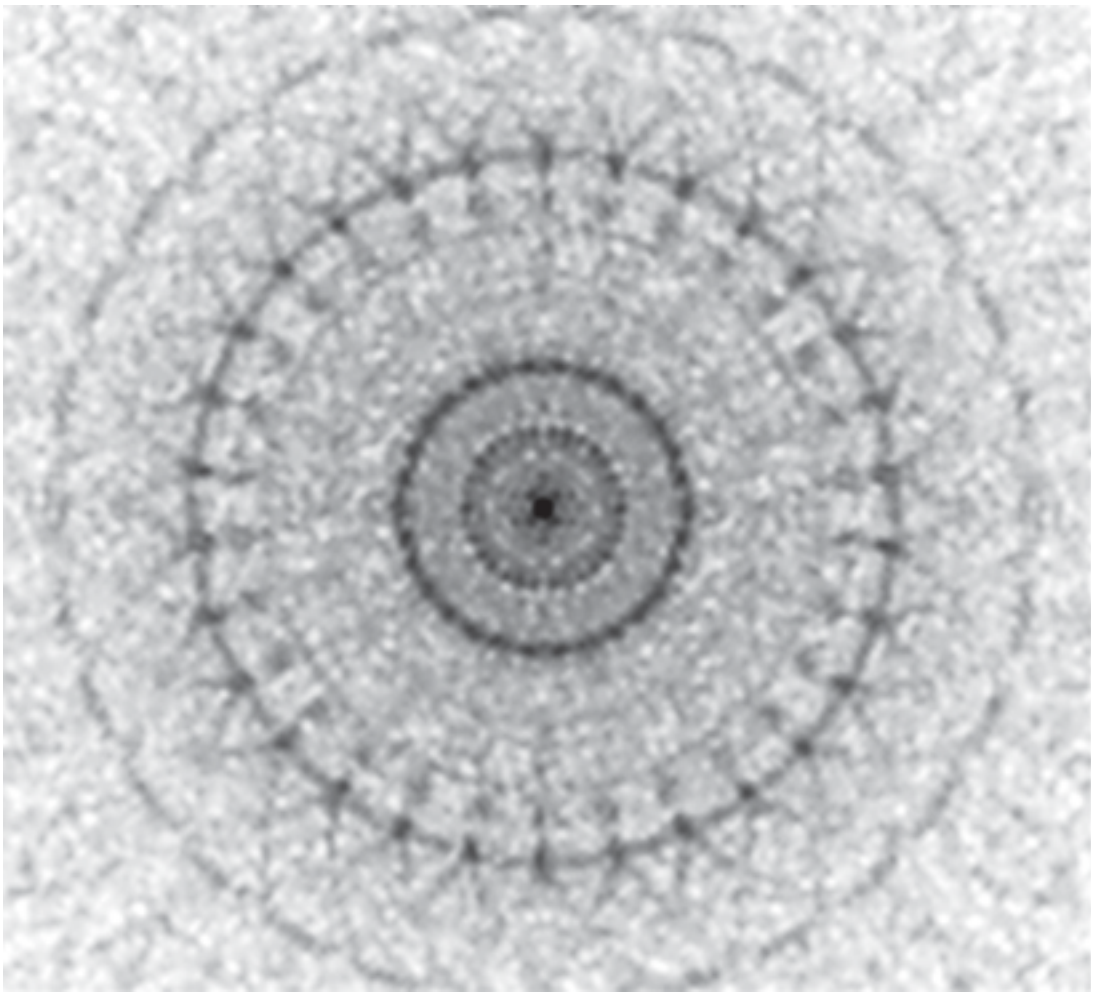

FIG. 20. Numerical Fourier transform (FT) of Dodony's model of 30-sectored polygonal serpentine (similar to Fig.13a in Dodony 1997a). This FT looks somewhat different from the experimental SAED patterns and from our simulated patterns (see text).

by a better centering of the SAED patterns when using convergent beam conditions. The above feature points to the fact that high-resolution, two-dimensional imaging is usually not obtained routinely all over the circumference of a fiber. The cylindrical, helical or conical nature of PS fibers, however, is best documented if observed along the [010] direction, and a systematic study in this zone axis should be considered to complete their description.

An additional argument to support the description of sector boundaries as glide dislocation walls is the observation of plastic deformation of 15- and 30-sector PS with sufficiently large inner holes were squeezed or bent (Fig. 21). As a matter of fact, the deformation of polygons is much more likely accommodated by the migration of walls of glide dislocations than by possible migration of polarity-reversal boundaries.

Fivefold symmetry of regular polygonal fibers

From the similar and symmetrical unit-cell sequences in the 15- and 30-sector PS, one could have inferred that the complete fibers display a fivefold symmetry for 15 sectors, and a misleading tenfold symmetry for 30 sectors, as indicated by the succession of ...|*LRO*|*LRO*... unit cells, or by electron-bombardment damage between or within sectors (Fig. 5). This is true in projection, but not true in the 3-D space. This statement comes from the centering of the basal, rectangular, *ab* unit-cell of serpentine. Along the fiber axis, direct-lattice rows carrying cell-corner lattice nodes ("subscript 1" below) and those carrying cell-centering lattice nodes ("subscript 2") alternate in a [100] projection along the basal plane. The two types of lattice nodes are shifted by *a*/2 along [100]. If one takes into account those two types, the unit-cell sequence of a 30-sector PS is ...|$L_1R_1O_1L_2R_2O_2$| $L_1R_1O_1L_2R_2O_2$... Hence there are six types of neighboring unit-cells around a fiber, and therefore the fiber axis is also a fivefold axis of symmetry for a 30-sector PS.

Fivefold symmetry around the fiber axis should thus be a general feature of normal chrysotile (Devouard & Baronnet 1993, Cressey & Whittaker 1993) and in addition of polygonal serpentines (Baronnet & Mellini

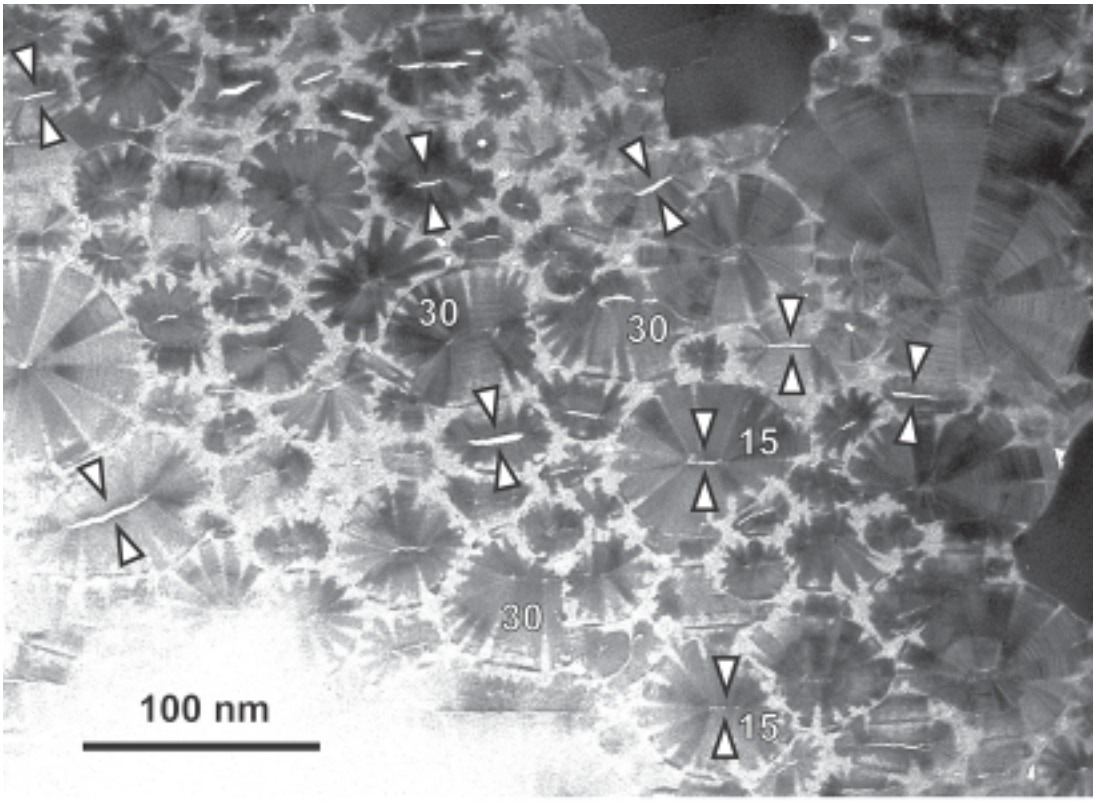

FIG. 21. Assemblage of intergrown 15-PS (15) and 30-PS (30) fibers, interpreted as having undergone plastic deformation. Sectors having layers normal to the expected compressive stress (N-S) are wider than the others (arrows). Collapsed hollow cores extend W-E as "mouths", especially in the case of large fibers. Piemont serpentinite, Western Alps, Italy.

1992, Baronnet *et al*. 1994, this work). For fibers with disordered sequences of stacking, this fivefold symmetry is still visible in direct space, repeating an identical disordered sequence five times a turn (see Devouard & Baronnet 1995, their Figs. 5 and 6), but it must be noted that this symmetry does not appear in diffraction space (Fig. 19) because different disordered sequences of stacking give rise to indistinguishable diffraction-intensities along diffraction streaks.

Conclusions

This work, which systematically combines observations in direct and in diffraction spaces and modeling of these features, places particular emphasis on the dual nature of the PS microstructure. Sectors are lizardite-like, with relationships between their stacking sequences insured by layer continuity across their boundaries. Boundaries themselves are shown to be made of curved parts of the layers with a unique radius of curvature. As a consequence, correct and periodic hydrogen bonding prevails inside sectors, whereas H-bonding is disturbed in the curved boundaries between sectors. Along these curved regions H-bonds are gradually distorted and lost. Such curved regions are accounted for by radial walls of partial dislocations. Each of these dislocations is "extended" or "delocalized" over the curved junction between layers. Assuming an average d(00*N*) = 0.724 nm for lizardite-like sectors (Mellini 1982, Mellini & Zanazzi 1987), curvature would cause the basal lattice-distance to increase continuously at junctions from *d*(00*N*) to *d*(00*N*)/cos(12°), *i.e.*, from 0.724 to 0.740 nm in 15-sector PS, and from *d*(00*N*) to *d*(00*N*)/cos(6°), *i.e.*, from 0.724 to 0.728 nm in 30-sector PS. Therefore, these curved parts of the PS microstructures cannot be compared to slabs of chrysotile for which the radius of curvature increases with central distance. This is a peculiarity of the PS structure. Accordingly, polygonal serpentines cannot be polysomatically described as a rose-like, alternating arrangement of lizardite and chrysotile.

Grauby *et al*. (1998) synthesized hydrothermally chrysotile from gels in the system SiO_2–MgO–H_2O, at constant a P(H_2O) of 700 bars and a T of 300°C, with different run-durations. One salient result has been to demonstrate that synthetic polygonal serpentines may form from cylindrical chrysotile once a critical diameter of fibers of *ca*. 50–100 nm is surpassed. Solid-state polygonization of the former cylindrical lattice is most probably taking place, then followed by inner growth and unlimited overgrowth on inner and outer polygon facets, respectively. Accordingly, in addition to transitions from curved layers to flat layers to form sectors, the polygonization of serpentine would seem to imply also an evolution of concentrically curved layers to equally curved layers to form sector boundaries.

ACKNOWLEDGEMENTS

The authors are indebted to S. Nitsche and D. Chaudanson for maintenance and optimization of TEM facilities at CRMC–N (CNRS–INSU French National facility), and to F. Quintric for some photographic work. E. Belluso, O. Oufi, R.F. Martin, G. Normand provided some, or helped sampling, of the vein serpentinite samples used here. G. van Tendeloo kindly permitted the use of the HRTEM pictures in Figures 3b and 4b taken with the JEOL 4000 EX at RUCA/EMAT (Antwerp) during the post-doc stay of one of us (BD). Particular gratitude is due to Robert F. Martin and Fred Wicks for their very careful editorial work and reviews, which considerably improved the manuscript. The constructive review by M. Mellini was much appreciated. Stimulating discussions with J. Banfield, C. Janot, and G. Ferraris were very helpful. A part of this work has been supported by the CNRS/INSU contract "Géomatériaux": 98 GEOMAT 09.

REFERENCES

AMELINCKX, S., DEVOUARD, B. & BARONNET, A. (1996): Geometrical aspects of the diffraction space of serpentine rolled microstructures: their study by means of electron diffraction and microscopy. *Acta Crystallogr.* **A52**, 850-878.

BAILEY, S.W. (1988): Polytypism of 1:1 layer silicates. *In* Hydrous Phyllosilicates (S.W. Bailey, ed.). *Rev. Mineral.* **19**, 9-27.

_____ & BANFIELD, J.F. (1995): Derivation and identification of non-standard serpentine polytypes. *Am. Mineral.* **80**, 1104-1115.

BARONNET, A. & BELLUSO, E. (2002): Microstructures of the silicates: key information about mineral reactions and a link with earth and materials sciences. *Mineral. Mag.* **66**, 709-732.

_____ & DEVOUARD, B. (1996): Topology and crystal growth of natural chrysotile and polygonal serpentine. *J. Crystal Growth* **166**, 952-960.

_____ & MELLINI, M. (1992): Polygonized serpentine as the first mineral with five-fold symmetry. *29th Int. Geol. Congress* (*Kyoto*) **3**, 682.

_____, _____ & DEVOUARD, B. (1994): Sectors of polygonal serpentine. A model based on dislocations. *Phys. Chem. Minerals* **21**, 330-343.

BELLUSO, E., BARONNET, A. & FERRARIS, G. (1998): Vein serpentinite textures from Western Alps, seen by HRTEM. *Int. Mineral. Assoc., 17th Gen. Meeting* (*Toronto*), *Programme and Abstr. Vol.*, A83.

CHISHOLM, J.E. (1991): Geometrical constraints on the growth of sectors in polygonal serpentine. *J. Phys., D: Appl. Phys.* **24**, 199-202.

_____ (1992): The number of sectors in polygonal serpentine. *Can. Mineral*. **30**, 355-365.

CRESSEY, B.A. (1979): Electron microscopy of serpentine textures. *Can. Mineral.* **17**, 741-756.

_____ & ZUSSMAN, J. (1976): Electron microscopic studies of serpentinites. *Can. Mineral.* **14**, 307-313.

_____ & WHITTAKER, E.J.W. (1993): Five-fold symmetry in chrysotile asbestos revealed by transmission electron microscopy. *Mineral. Mag.* **57**, 729-732.

DEVOUARD, B. (1995): *Structure et croissance cristalline du chrysotile et des serpentines polygonales*. Thèse de doctorat, Université d'Aix-Marseille III, Marseille, France.

_____ & BARONNET, A. (1993): Five-fold symmetry in chrysotile. EUG VII (Strasbourg). *Terra Abstr., Terra Nova* **5** (suppl.), 351.

_____ & _____ (1995): Axial diffraction of curved lattices: geometrical and numerical modeling. Application to chrysotile. *Eur. J. Mineral.* **7**, 835-846.

_____, _____, VAN TENDELOO, G. & AMELINCKX, S. (1997): First evidence of synthetic polygonal serpentines. *Eur. J. Mineral.* **9**, 539-546.

DODONY, I. (1993): Microstructures in serpentinites. *Microscopia Elettronica* **14**(2) *Suppl*., 249-252.

_____ (1997a): Structure of the 30-sector polygonal serpentine. A model based on TEM and SAED studies. *Phys. Chem. Minerals* **24**, 39-49.

_____ (1997b): Theoretical derivation and identification of possible two-layer lizardite polytypes. *In* Modular Aspects of Minerals (S. Merlino, ed.). *Eur. Mineral. Union, Notes in Mineralogy* **1**, 57-80.

GRAUBY, O., BARONNET, A., DEVOUARD, B., SCHUMAKER, K. & DEMIRDJIAN, L. (1998): The chrysotile – polygonal serpentine – lizardite suite synthesized from a 3 MgO – 2 SiO_2 – excess H_2O gel. Eur. Mineral. Petrol. Geochem. (EMPG VII). *Terra Nova*, *Suppl.* **10**(1), 24 (abstr.).

GUTHRIE, G.D., Jr. & VEBLEN D.R. (1990): Interpreting one-dimensional high-resolution transmission electron micrographs of sheet silicates by computer simulation. *Am. Mineral.* **75**, 276-288.

JAGODZINSKI, H. & KUNZE, G. (1954): Die Rollchen-struktur des Chrysotils. I. Allgemeine Beugungstheorie und Kleinwinkelstreuung. *Neues Jahrb. Mineral., Monatsh.*, 95-108.

JIANG, S. & LIU, W. (1984): Discovery and its significance of povlen type hydrochrysotile. *Acta Geol. Sinica* **58**(2), 136-142 (in Chinese, with English abstr.).

MELLINI, M. (1982): The crystal structure of lizardite 1T: hydrogen bonds and polytypism. *Am. Mineral.* **67**, 587-598.

_____ (1986): Chrysotile and polygonal serpentine from the Balangero serpentinite. *Mineral. Mag.* **50**, 301-306.

_____ & ZANAZZI, P.F. (1987): Crystal structures of lizardite-1T and lizardite-$2H_1$ from Coli, Italy. *Am. Mineral.* **72**, 943-948.

MIDDLETON, A.P. & WHITTAKER, E.J.W. (1976): The structure of Povlen-type chrysotile. *Can. Mineral.* **14**, 301-306.

MITCHELL, R.H. & PUTNIS, A. (1988): Polygonal serpentine in segregation-textured kimberlite. *Can. Mineral*. **26**, 991-997.

PAPP, G. (1988): *Mineralogical Study of Serpentines with a Special View to the Occurrences in Hungary*. Doctoral thesis, Eötvös Lorand Univ., Budapest, Hungary.

_____ (1990): A review of the multi-layer lizardite polytypes. *Annls. Hst.-Nat. Mus. Natn. Hung.* **82**, 9-17.

SPINNLER, G.E. (1985): *HRTEM Study of Antigorite, Pyroxene–Serpentine Reactions, and Chlorite*. Ph.D. thesis, Arizona State Univ., Tempe, Arizona.

WICKS, F.J. & O'HANLEY, D.S. (1988): Serpentine minerals: structures and petrology. *In* Hydrous Phyllosilicates (S.W. Bailey, ed.). *Rev. Mineral*. **19**, 91-167.

YADA, K. (1967): Study of chrysotile asbestos by a high resolution electron microscope. *Acta Crystallogr.* **23**, 704-707.

_____ (1971): Study of microstructure of chrysotile asbestos by high resolution electron microscopy. *Acta Crystallogr.* **A27**, 659-664.

_____ & LIU, W. (1987): Polygonal microstructures of Povlen chrysotile observed by high resolution electron microscopy. *Proc. Sixth Meet., Eur. Clay Group* (*Sevilla*), 596-597 (abstr.).

Received March 15, 2004, revised manuscript accepted November 2, 2004.

APPENDIX: RECIPROCAL SPACE OF CURVED SECTOR-BOUNDARIES

We suppose that, in direct space, the junctions between successive planar sectors are made of a portion of cylinder each, stacked along the sector boundary (Fig. A1a). In projection along the fiber axis, straight "lattice" lines of adjacent sectors are linked by identical circular arcs. The direct object is generated through iterative displacement of one set of "arc + two adjacent lines" shifted by D along the boundary, such that the lattice spacing t in flat sectors obeys: $D = t / \cos(\pi/n)$, with n as the number of sectors in the fiber (15 or 30).

For the pile of arcs, the diffraction pattern is seen as the set of tips of diffraction vectors issued from the set of parallel and δ-equidistant tangents to the arcs, considering a β angle variation between $-\pi/n$ and $+\pi/n$: $\delta = D \cos\beta = t \cos\beta / \cos(\pi/n)$.

In the range $-\pi/n \le \beta \le +\pi/n$, the locus of the tip of diffraction vectors may be expressed in polar coordinates as: $1/\delta = \cos(\pi/n) / t \cos\beta = \text{cst} / \cos\beta$. This is the polar equation of a linear segment normal to the $\beta = 0$ symmetry line and ending at $(\pm \pi/n; 1/t)$, *i.e.*, connecting basal reflections (Fig. A1b).

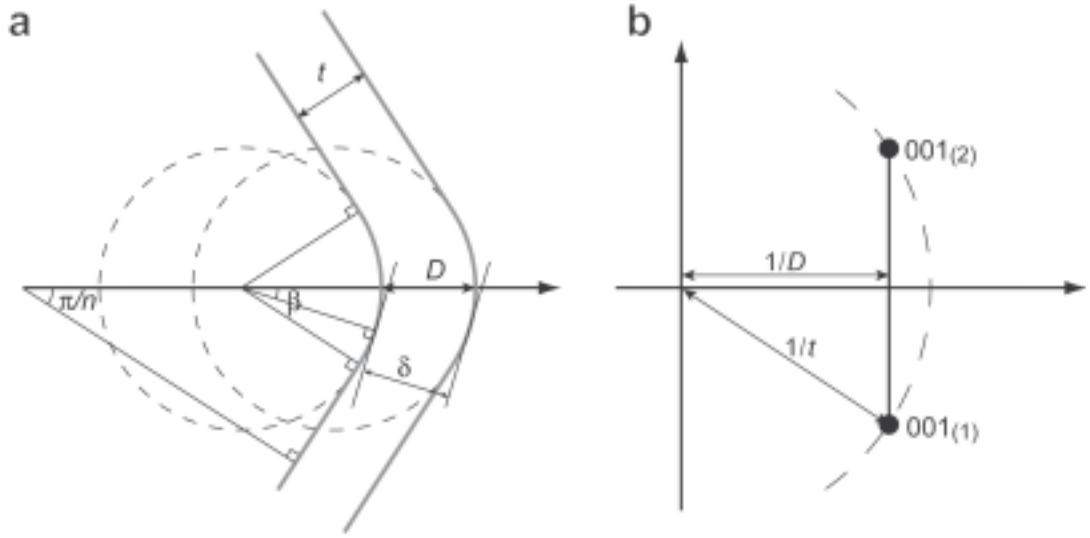

FIG. A1. a) Schematic drawing of two successive lattice-planes crossing a curved sector-boundary. b) Its transform in reciprocal space.